# Cooling with a subsonic flow of quantum fluid

Pantxo Diribarne, Bernard Rousset, Yuri A. Sergeev, Camille Noûs, Jérôme Valentin, Philippe-E. Roche

# Cooling with a subsonic flow of quantum fluid

Pantxo Diribarne* and Bernard Rousset
*Univ. Grenoble Alpes, CEA IRIG-DSBT, 38000 Grenoble, France*

Yuri A. Sergeev
*Joint Quantum Centre Durham-Newcastle, School of Mathematics, Statistics and Physics, Newcastle University, Newcastle upon Tyne, NE1 7RU, UK*

Camille Noûs
*Laboratoire Cogitamus, France*

Jérôme Valentin† and Philippe-Emmanuel Roche
*Univ. Grenoble Alpes, CNRS, Institut NEEL, F-38042 Grenoble, France*

Miniature heaters are immersed in flows of quantum fluid and the efficiency of heat transfer is monitored versus velocity, superfluid fraction and time. The fluid is $^4$He helium with a superfluid fraction varied from 71% down to 0% and an imposed velocity up to 3 m/s, while the characteristic sizes of heaters range from 1.3 $\mu$m up to a few hundreds of microns. At low heat fluxes, no velocity dependence is observed, in agreement with expectations. In contrast, some velocity dependence emerges at larger heat flux, as reported previously, and three nontrivial properties of heat transfer are identified.

First, at the largest superfluid fraction (71%), a new heat transfer regime appears at non-null velocities and it is typically 10% *less* conductive than at zero velocity. Second, the velocity dependence of the mean heat transfer is compatible with the square-root dependence observed in classical fluids. Surprisingly, the prefactor to this dependence is maximum for an intermediate superfluid fraction or temperature (around 2 K). Third, the heat transfer time series exhibit highly conductive short-lived events. These *cooling glitches* have a velocity-dependent characteristic time, which manifest itself as a broad and energetic peak in the spectrum of heat transfer time series, in the kHz range.

After showing that the velocity dependence can be attributed to the breaking of superfluidity within a thin shell surrounding heaters, an analytical model of forced heat transfer in a quantum flow is developed to account for the properties reported above. We argue that large scale flow patterns must form around the heater, having a size proportional to the heat flux (here two decades larger than the heater diameter) and resulting in a turbulent wake. The observed spectral peaking of heat transfer is quantitatively consistent with the formation of a Von Kármán vortex street in the wake of a bluff body nearly two decades larger than the heater but its precise temperature and velocity dependence remains unexplained. An alternative interpretation for the spectral peaking is discussed, in connection with existing predictions of a bottleneck in the superfluid velocity spectra and energy equipartition.

## I. INTRODUCTION AND MOTIVATION

Below its superfluid transition temperature, liquid helium $^4$He enters the He II phase which displays amazing quantum properties at large scales [1]. In particular, this fluid can flow without viscous friction, it hosts propagating heat waves – called second sound waves – and is extremely efficient in transporting heat.

Quantum fluids [2] such as He II are also characterized by the existence of quantized vortex filaments which concentrate all the vorticity of the superfluid [3]. Although the presence of superfluid vortices reduces the efficiency of heat transport, the latter remains much more efficient than standard convection and diffusion heat transport in most situations [4].

A famous model to describe heat transport and hydrodynamics of quantum fluids at finite temperature is Tisza and Landau's two-fluid model, which describes He II as an intimated mixture of an inviscid *superfluid component* and a viscous *normal component* that contains all the entropy of the fluid [5]. The local relative density fraction of both components depends on the local temperature.

Thus, steady heat transport can be described as a flow of normal component carrying its entropy. When this mass flow is balanced by an opposite mass flow of superfluid, we have a so-called *thermal counter-flow*. This situation occurs, for instance, in the vicinity of heaters and coolers, and it has been extensively studied in pipe and channel geometries [4].

Contrary to the situation in classical fluids, forced convection in He II has long been assumed not to improve measurably heat transfer, because the classical convection and diffusion mechanisms are far less efficient than counter-flows in transporting heat, at least in subsonic flows. The special case of flows reaching or exceeding the

* pantxo.diribarne@univ-grenoble-alpes.fr
† present address LERMA, Observatoire de Paris, 75014 Paris

velocity of second sound, or even first sound in helium (typically 16.5 and 227 m/s at 2 K) is not addressed in the present study, nor in others to the best of our knowledge.

Yet, in a recent instrumental study, Durì *et al.* [6] reported that an external (subsonic) flow can favor heat transfer from a hot-wire, but the underlying mechanism was not addressed.

This paper reports en experimental study of forced heat transfer from heaters immersed in a subsonic flow of superfluid, and reveals a rich phenomenology.

Related previous studies are reviewed in Sec. II. The experiments are presented in Sec. III, in particular the subsonic flows and the various miniature heaters used. Sections IV, V and VI report three key properties of forced heat transfer in He II: the existence of metastable conduction states, velocity and temperature dependencies of heat transfer, and the existence of short-lived cooling events, named cooling glitches. Section. VII presents analytical models accounting for some – but not all – observations.

## II. STATE OF THE ART

In the absence of an external flow, He II heat transfer studies are often reported in the thermal counter-flow literature. In particular, the modeling of nonplanar geometries has recently been the subject of a number of numerical and theoretical studies, most of which predict non trivial behaviors.

Saluto *et al.* [7] have used a so-called *hydrodynamical model* [8] to assess the behavior of the vortex line density of a counter-flow between two concentric cylinders at different temperatures. From their initial model they derived a modified Vinen equation which, in addition to the original source and sink terms, features a vortex diffusion term. In the presence of a nonuniform heat-flux, the model predicts a nonuniform vortex line density (as does the original Vinen model) with a diffusive migration of vortices produced in the most dense region to the most dilute region. The main consequence of this addition is that if the heat flux is varied faster than the typical diffusion time, the local vortex line density has an hysteretic behavior.

Using the vortex filament method Varga [9] has shown that in spherical geometry (using a point source), for bath temperatures larger than 1.5 K, all initial seeding vortices are annihilated on the virtual heat source. For smaller temperatures, a self-sustained vortex tangle was generated but, due to computational limitations, it could not reach a stationary state. Inui and Tsubota [10] have run a similar numerical simulation with a different approach for the core: instead of a point source, they simulated an actual spherical heater (of a finite diameter) using suitable boundary conditions for the normal and superfluid velocities. Contrary to Varga [9] they show that they are able to obtain a self-sustained vortex tangle at most temperatures, with a non trivial density profile.

Rickinson *et al.* [11] used the same vortex filament method to model the vortex tangle of a cylindrical counter-flow, with a finite inner diameter. What they find is that in order to reach a stationary state, they need to specify a radius dependent friction parameter between the two components of He II (which somewhat mimics the effect of an actual temperature gradient). The latter trick was inspired by a previous finding [12], that showed that using the coarse-grained Hall-Vinen-Bekarevich-Khalatnikov (HVBK) model it was necessary to take the variations of the fluid properties around the wire into account, in order to reach a stationary state in cylindrical geometry. Rickinson *et al.* [11] showed the standard scaling for the vortex line density $\mathcal{L}$ as a function of the relative velocity $v_{ns}$ between the two components holds: $\mathcal{L} \propto v_{ns}^n$ with $n \approx 2$. This is an important result in that it allows for the use of standard macroscopic laws for the heat transfer around non planar surfaces. Among others, it supports *a posteriori* the use of the conduction function when simulating the heat flux around a cylindrical heater [6].

Now we turn to the problem of heat transfer in He II in the presence of an external flow, for which the literature is much sparser. First, two experimental studies in pipe flows are worth mentioning. Johnson and Jones [13] have measured the heat flux through a tube in the presence of both temperature and pressure gradients and concluded that the presence of a pressure driven flow inside the tube somewhat increased the mutual friction between the superfluid and normal components, thereby depleting the efficiency of the heat transfer. Rousset *et al.* [14] measured the temperature profile around a heater that was placed in the middle of a tube traversed by a subsonic He II flow. They were able to account for most of the results using simple entropy conservation model and isenthalpic expansion corrections (see also Refs. [15–17]).

A third experimental observation is directly related to the present one. In an instrumentation study, Durì *et al.* [6] reported that an external flow increases the heat transfer around a hot-wire anemometer, which is basically an overheated wire-shaped thermometer. They were able to account quantitatively for the heat transfer at null velocity assuming that standard counter-flow laws still hold in cylindrical geometry despite very high heat flux, but did not propose any explanation for the heat transfer improvement due to the external flow.

To the best of our knowledge, there has not been any attempt at studying specifically the effect of an external flow on the heat transfer at the interface between a solid body and He II. This paper attempts to fill these gaps in our understanding of heat transfer in superfluid flows.

## III. EXPERIMENTAL CONDITIONS

This study uses three different miniature heaters immersed in flows of He II to assess the properties of intense

| Heater | Facility / Flow | $P$ [bar] | $v_\infty$[m/s] | $T_\infty$ [K] | $X_{sf}$[%] |
|---|---|---|---|---|---|
| Wire | HeJet / grid flow | 2.6 | 0 - 0.40 | 1.74 | 71 |
| | | | 0 - 0.52 | 1.93 | 51 |
| | | | 0 - 0.52 | 2.05 | 31 |
| | | | 0 - 0.52 | 2.13 | 10 |
| | | | 0 - 0.52 | 2.29 | 0 |
| Film | HeJet / grid flow | 2.6 | 0.38 | 2.00 | 40 |
| Chip | SHREK / rotating flow | 3.0 | 0 - 3 (0 - 1.2 Hz) | 1.6 - 2.1 | 82 - 20 |

TABLE I. Summary of experimental conditions for all heaters. Here $v_\infty$ and $T_\infty$ are, respectively, the fluid velocity and temperature away from the heater. The density fraction of superfluid component $X_{sf}$ is estimated in pressurized helium using the HEPAK® library.

heat transfer in subsonic quantum flows.

In the following we first describe the measurement protocol and then provide the detailed description of the flows and, finally, of the heaters.

The experimental conditions are summarized in Table I.

### A. Measurement principles.

The heat flux from the heaters is produced by the Joule effect, $\dot{Q} = eI = RI^2$, where $e$ is the voltage across the heater, $I$ is the current through it, and $R$ is its electrical resistance. The spatially averaged temperature of the heater $T_w$ is inferred from the calibration law $R(T_w)$ of its temperature-dependent resistance. The heaters can thus be considered as overheated thermometers. Their different shapes and sizes are described in Sec. III C.

In order to monitor the fluctuations of the heat transfer, two types of electronics circuitry are used to drive the heaters: constant-current sources and a constant-resistance (or temperature) controller. The latter is a commercial hot-wire anemometry controller able to control the resistance over a bandwidth exceeding DC-30 kHz (DISA model 55-M10). The measured voltage $e$ is either the voltage drop across the heater when using the constant current circuit, or an image of the current through the heater (via a shunt resistance) when using the constant resistance controller. In both cases, time series are calculated for the total heat flux $\dot{Q}$ and the heater overheating $T_w - T_\infty$ with respect to the fluid temperature away from the heater, $T_\infty$.

The use of two types of electronics allows us to check if the observed instabilities are artifacts associated with the electronic circuitry. The signals are acquired by a delta-sigma analog-to-digital converter (NI-PXI4462), at sampling frequencies up to 100 kHz (most often 30 kHz). For given flow conditions, the typical data set consists of 15 files with $4 \times 10^6$ data samples.

### B. Descriptions of the flows

Two facilities in Grenoble, SHREK and HeJet, are used to produce pressurized flows with a steady mean velocity and limited turbulent fluctuations. The pressurization of the flow above the fluid critical pressure is required to prevent boiling or the formation of a gas film around the heater irrespective of the amount of overheating.

In mechanically-driven isothermal turbulent flows, such as those produced by both facilities, the superfluid and the normal fluid components that make up He II are locked together at large and intermediate flow scales [18, 19]. In the quantum turbulence literature, such flows are sometimes referred to as co-flows, to distinguish them from the thermally driven He II flows, called counter-flows. Surely, as discussed later, the flow in the close vicinity of the heater is no longer a co-flow.

In the following subsections we give the most important details about the HeJet facility where most measurements were done using the two smallest heaters, and the SHREK facility, in which measurements with the largest heater were performed.

#### *1. HeJet: The grid flow*

The HeJet facility is a closed loop of pressurized liquid helium immersed in a liquid helium bath at saturated pressure (dark gray in Fig. 1). The flow in the loop is driven by a centrifugal pump empowered by a DC motor at room temperature. The facility, originally designed to produce an inertial round jet of liquid helium [20], has been modified to produce a turbulent grid flow (see Fig. 1). The motivation for this change was to obtain a quantum flow with relative velocity fluctuations $I$ within a few percents.

The experimental flow section consists of a $32\times32\,\mathrm{mm}^2$ square cross section tunnel with length 450 mm. Prior to entering the tunnel, the flow goes through the conditioning section: a divergent (32 mm to 50 mm round section) followed by a 16 mm long honeycomb with 3 mm mesh size and then a convergent part which smoothly concentrates the flow into the square tunnel section.

The grid is etched by wire electro-erosion in a 0.8 mm thick stainless steel plate. The rods are thus 0.8 mm × 0.8 mm wide and the mesh size is $M = 4$ mm which leads to a solidity (or obstruction ratio) of 36%. The geometry of the grid follows the now standard recommendations from Comte-Bellot and Corrsin [21].

Measurements are done at a distance of 60 $M$ downstream the grid. At this location, the longitudinal integral length scale is $L_f = 5.0 \pm 0.2$ mm and the turbulence intensity, defined as the ratio of the root-mean squared fluctuating velocity $v'$ to the mean velocity $v_\infty$,is $I \approx 2.6\%$. The procedure for characterizing the flow is detailed in the Appendix.

The range of explored temperatures is 1.74 K to 2.28 K, corresponding to a superfluid fraction from 71% to 0%.

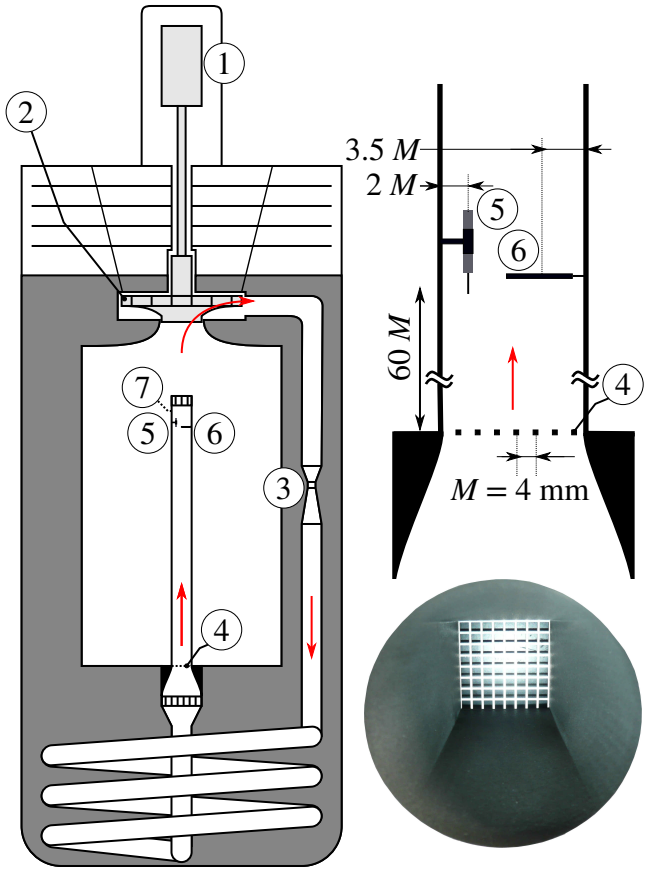


FIG. 1. Left: Sketch of the experimental apparatus. **1**: DC motor. **2**: Centrifugal pump. **3**: Venturi flow-meter. **4**: Grid. **5**: Pt-Rh wire heater. **6**: Film heater array. **7**: Temperature sensor. Right: zoom of the test section with relevant dimensions and a picture of the convergent followed by the grid.

The temperature in the pressurized bath is measured at the outlet of the grid flow tube (see Fig. 1) with a Cernox® thermometer and is regulated by means of a heater within a few tenths of milliKelvin. The absolute value of the temperature, known to better than 1 mK, is checked *in situ* using the saturated pressure of the (superfluid) outer bath when the pressurized flow is at rest.

The range of mean velocities is $v_\infty = 0$ to 0.52 m/s, as calculated from the Venturi flow-meter pressure drops (see item 3 in Fig. 1).

For all experiments, the pressure is maintained at $2.6 \pm 0.1$ bars. In such condition, the superfluid transition occurs at $T_\lambda \approx 2.15$ K.

#### 2. SHREK: The rotating flow

SHREK is a large cylindrical vessel, $D_s = 78$ cm in inner diameter and 116 cm in height, equipped with two identical turbines facing each other (see Rousset *et al.* [22] for details). The turbines are fitted with curved blades so that, depending on their respective rotation direction, the facility can produce different kinds of flows: from the quasi solid rotation flow when turbines rotate in the same direction (co-rotation), to the von Kármán flow when turbines rotate in opposite directions (counter-rotation).

In this paper we report data acquired in co-rotation from a bare chip heater (see Sec. III C 3) located in the mid plane of the vessel, 1 cm away from the wall. This sensor was previously used as an anemometer in He I (see Fig. 14 in Ref. [22]). In those co-rotation conditions, the turbulence intensity was found to be of the order 5%.

In order to estimate the velocity of the fluid around the sensor, we assume that the co-rotation produces a solid-body rotation flow with the same angular velocity $\omega$ as the turbines: $v_\infty = \omega D_s/2$. This simple model probably slightly overestimates the velocity but it gives an order of magnitude of the velocity with sufficient accuracy for the purpose of the current study.

The flow pressure is maintained at 3 bars to avoid boiling and cavitation on the miniature heaters. In such conditions, the superfluid transition occurs also at $T_\lambda \approx 2.15$ K.

### C. Description of the miniature heaters

#### 1. The wire

The wire heater is made of a 90% platinum – 10% rhodium alloy. It is manufactured from a Wollaston wire by etching its 50 $\mu$m-diameter silver cladding. The wire diameter, as documented by the manufacturer, is $d_w = 1.3\,\mu$m and its length is estimated from resistance measurements to be 450 $\mu$m. It is essentially built the same way as it was in Durì *et al.* [6] and the main difference is that the present wire is soldered on a DANTEC 55P01 hot-wire support.

The resistivity of the Pt-Rh alloy decreases almost linearly with the temperature from 300 K down to 40 – 50 K, and the sensitivity, $dR_w/dT$, where $R_w$ is the wire's resistance, is therefore almost constant. Below this temperature, the sensitivity starts to decrease until it eventually vanishes around 13 K. For this reason it is necessary to maintain the wire at temperatures well above 13 K, in order to have access to its temperature through the resistance measurement. We typically overheat it to $T_w \approx 25$ K which corresponds $R_w \approx 36\,\Omega$.

The wire heater is driven at constant resistance and thus at constant temperature.

#### 2. The film

The film heater consists of a platinum thin-film strip, patterned within a $2.6\,\mu\text{m} \times 5\,\mu$m area, and deposited on a 500 nm-thick, 10 $\mu$m-wide and 1 mm-long SiN ribbon (see Fig. 2). The current leads to the Pt strip consist of 200 nm gold layers. As previously for the Pt-Rh alloy of

the wire heater, the temperature sensitivity of Pt electrical resistivity vanishes around 13 K [23]. In practice, the heater is overheated up to few tens of Kelvins to benefit from a nearly temperature-independent sensitivity. Without overheating, the resistance of the film is 730 Ω below 10 K and 1060 Ω at 77 K. To reach an overheating of 25 K in a quiescent 2 K He II bath, a current of 300 $\mu$A is needed. Details about the microfabrication process of this probe will be provided in another paper.

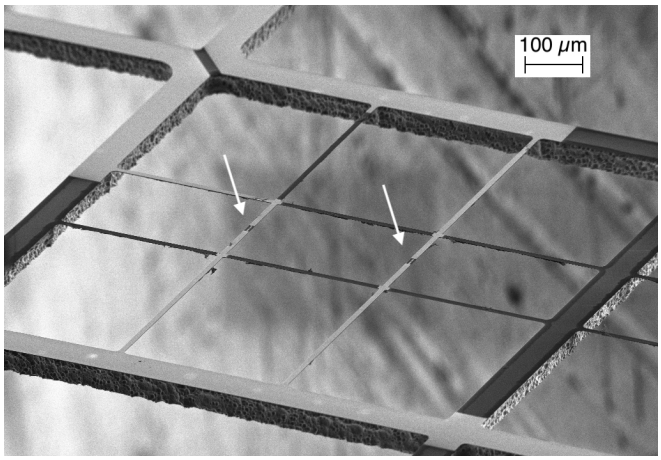


FIG. 2. Electron microscope picture of the frame holding the film heater array. Two heating Pt strips are dark areas, pointed by white arrows, near the center of the supporting 1-mm-long SiN ribbons. A gold layer deposited on both sides of Pt provides the electrical contacts (lighter area). Thermal contact between Au and the Pt strip is reduced thanks to an intermediate buffer of Pt.

This heating film is mounted in the grid flow – with the film facing upstream – and driven with a constant-current electronics.

#### 3. *The chip*

The chip heater is a bare Cernox® CX-BR thermometer from Lake Shore cryotronics Inc., mounted in the SHREK experiment. It consists of a 0.3 $\mu$m thick zirconium oxynitride film deposited on a sapphire substrate whose dimensions are 0.2 mm × 0.97 mm × 0.76 mm [24].

Like semiconductors, and contrary to Pt-Rh and Pt heaters, the resistance increases as the temperature decreases. The sensitivity $(T/R)dR/dT$ remains almost constant $(-0.45 \pm 0.05)$ over the explored temperature range, from 1.7 K to 30 K. This contrasts with the two previous heaters which lose temperature sensitivity below roughly 13 K.

The probe is driven at slowly varying sinusoidal current $i(t)$:

$$i(t) = I_0 \sin\left(2\pi \frac{t}{\tau}\right), \qquad (1)$$

where $I_0$ is the current amplitude and $\tau$ is the period. The resulting voltage $e$ across the chip together with the current are recorded using a NI-PCI-4462 acquisition board.

The period $\tau$ is typically 0.2 s, much larger than the thermal time constant of the chip and than the turnover time of large eddies in the flow. This allows us to determine continuously the temperature of the chip as a function of the input power, from bath temperature to around 30 K.

## IV. METASTABLE HEAT TRANSFER STATES AT LOW TEMPERATURE

At the lowest temperature explored in this study, $T_\infty = 1.74$ K which corresponds to a superfluid fraction of 71%, we report the observation of two metastable heat-transfer regimes. As the external velocity over the wire heater increases, the less conductive regime takes precedence over the more conductive one, in terms of residence time in each metastable state.

This effect manifests itself as a *decrease* of the averaged heat transfer as velocity increases, at least in the intermediate range of velocity where both co-exist. Rather than focusing on the average heat transfer, this effect is better illustrated by the histograms of the instantaneous heat transfer.

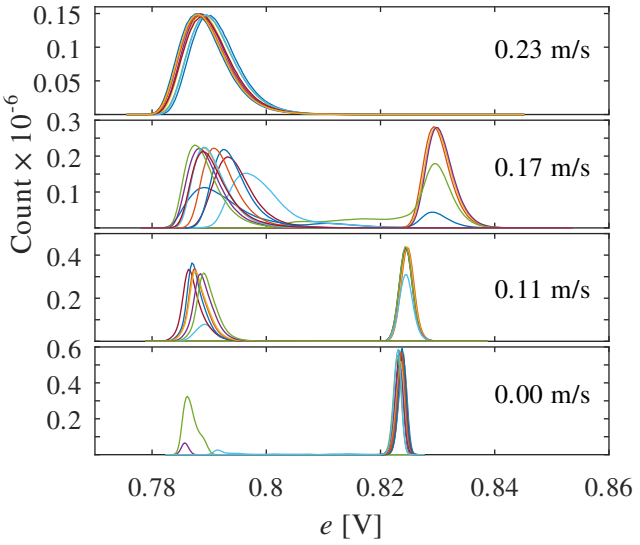


FIG. 3. Histogram of the wire heater voltage output at $T_\infty = 1.74$ K for various velocities. Each curve represents a dataset with $4 \times 10^6$ samples.

Figure 3 presents the histogram of the wire heater voltage at the four smallest velocities. Each curve is the histogram for one dataset, an approximately two-minutes-long segment of signal. This duration is much longer than the longest characteristic time scales of turbulence at the heater location; these time scales are

of the order of only a fraction of a second (typically $M/v_\infty \lesssim 4\,\mathrm{mm}/0.1\,\mathrm{m\,s^{-1}} \approx 0.04\,\mathrm{s}$). In this regard, a segment of any signal's segment that belongs to one of the conduction states can be considered quasistationary as far as hydrodynamic phenomena are concerned, and the corresponding states can be considered as stable or metastable. It cannot be fully excluded, though, that the switching from one state to the other is triggered by very rare events in the flow.

At null velocity, the more conductive state is clearly the most probable and as the velocity is increased the probability of observing this state progressively decreases and eventually vanishes. In the present conditions, the difference in heat transfer efficiency between the two states is around 10% and both states co-exist for $v_\infty \lesssim 0.2\,\mathrm{m/s}$. Analysis of the time series (not shown here) shows that the typical lifetime of each state is of the order of tens of seconds. For this reason, the two-state behavior described here should not be confused with that described below in Sec. VI B for the film heater signal. In the latter case, no metastable behavior will be observed: The persistence time of the most conductive state will be typically four to five decades shorter, and of the order of the shortest resolved time scale of the turbulence.

In the following section, which addresses the mean heat transfer versus mean velocity, the velocity response of each state will be examined separately.

## V. EFFECT OF THE VELOCITY ON THE MEAN HEAT TRANSFER

In this section we analyze the sensitivity of the mean heat transfer to the velocity of the surrounding flow. Using the chip heater, we first show that the sensitivity is conditioned to the presence of an He I film at the surface of the heater. Then we use the wire heater to determine how the temperature of the surrounding He II affects the sensitivity to the velocity.

### A. Sensitivity to velocity conditioned to the presence of an He I film

We report here that the heat transfer from a heater immersed in He II becomes velocity dependent concomitantly with the formation of an He I film around the heater.

Figure 4(a) shows the power required to overheat the chip heater in the absence of an external flow.

As expected, at the lowest power input, below approximately $10\,\mu$W, the chip temperature $T_{\mathrm{chip}}$ is close to the bath temperature $T_\infty$. This part of the curve is not detailed.

For power inputs larger than $10\,\mu$W, the chip temperature is measurably larger than the bath temperature. At intermediate power inputs exceeding $10\,\mu$W the curves for all bath temperatures tend to collapse on a single baseline curve, but for larger power inputs, above a bath temperature dependent critical power $\dot{Q}_{\mathrm{crit}}$, the chip temperature starts to increase with $\dot{Q}$ much more rapidly.

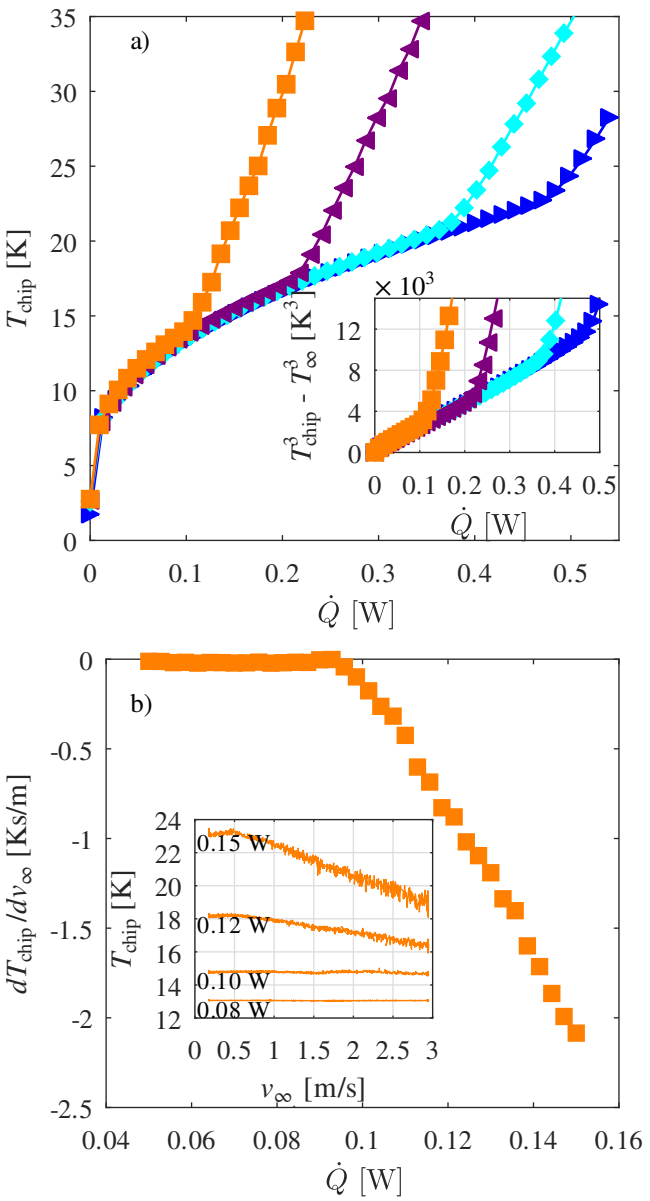


FIG. 4. a) Temperature $T_{\mathrm{chip}}$ of a bare chip Cernox® as a function of the dissipated electrical power for various bath temperatures: ■ 2.11 K, ◀ 2.05 K, ♦ 1.93 K, ▶ 1.74 K. Inset: $T^3_{\mathrm{chip}} - T^3_\infty$ as a function of $\dot{Q}$.
b) Average sensitivity of the temperature of the chip to the velocity in the range $1 - 1.5\,\mathrm{m/s}$ as a function of the input power. Inset: Temperature of the chip as a function of the velocity for various dissipated electrical powers. The temperature of the bath is $T_\infty = 2.11\,\mathrm{K}$, corresponding to the orange curve in panel (a).

As illustrated by the inset of Fig. 4(a), the temperature baseline common for of all curves in the intermediate power range evolves roughly as $T^n_{\mathrm{chip}} - T^n_\infty \propto \dot{Q}$ with

$n = 3$. Such a dependence is typical of a heat transfer limited mostly by a large-heat-flux Kapitza resistance. For instance Van Sciver compilation reports exponents of $n = 3 \pm 0.5$ (see p. 293 in Ref. [4]). This thermal resistance appears at the interface between the chip and helium, and at the inner solid interfaces within the chip. It is responsible for a significant overheating of the chip ($T_{\rm chip}$) compared to the liquid helium in contact with it ($T'_{\rm chip}$) [25].

With this in mind, the critical heat flux $\dot{Q}_{\rm crit}$ is interpreted as the threshold at which the temperature $T'_{\rm chip}$ of helium at the solid-liquid interface becomes larger than $T_\lambda$. Above this threshold, a thin He I layer forms around the heater. Since He I is significantly less conductive than He II, the chip temperature grows much more rapidly as the heat flux is increased beyond $\dot{Q}_{\rm crit}$. A similar phenomenology is reported in the "film boiling" literature when a heater is overheated in a bath of He II at saturated vapor pressure, instead of a bath of pressurized helium in our case. In this case, a helium gas layer forms around the heater and also contributes to thermal isolation of the heater from its surrounding.

Figure 4(b) presents an important result. In the inset, the heater's mean temperature is displayed versus the mean velocity of the surrounding flow at $T_\infty = 2.11\,\mathrm{K}$ (20% superfluid fraction). In the main axes, the average sensitivity $dT_{\rm chip}/dv_\infty$ in the velocity range from 1 to 1.5 m/s is displayed as a function of the input power. At the lowest heater power, no velocity dependence is discernible. This absence of sensitivity is observed down to 1.74 K, the lowest tested bath temperature, and is consistent with the standard understanding of heat transfer in He II [13]. Above $\dot{Q} \approx 0.093\,\mathrm{W} \approx \dot{Q}_{\rm crit}$, some sensitivity starts to develop. In other words, the observed velocity sensitivity is concomitant with the appearance of the He I layer surrounding the heater. As the power increases, the He I layer is expected to thicken thus leading to an increase, observed in our experiment, of the magnitude of sensitivity.

### B. Velocity-Temperature dependence of heat transfer

The chip heater, described above in Sec. III, is not well-suited to explore experimentally the basic mechanism of forced heat transfer. First, due to its "large" size and the sharp angles of its parallelepiped shape, its wake is highly turbulent at all velocities, which complicates modeling. Second, it is assembled with different materials leading to a larger Kapitza resistance and larger temperature inhomogeneity within the heater and thus at its surface. Third, its shape does not have any simple symmetry which could ease analytical description of heat transfer. Other limitations arise from the flow facility as it is not optimized to produce low velocity and thus a less turbulent wake on the heater. Besides, the velocity field in the vicinity of the heater is poorly known.

For all these reasons, systematic measurements have been performed in the grid flow using the wire heater. In these conditions the flow of He I over the wire can be regarded as laminar: its characteristic Reynolds number $\mathrm{Re} = d_w v_\infty/\nu$, with $d_w = 1.3\,\mu$m, $v_\infty = 0.2\,$m/s, and $\nu = 2\times10^{-8}\,\mathrm{m^2\,s^{-1}}$, is of the order of 10. In contrast, the corresponding Reynolds number of the flow around the chip heater is three decades larger, well beyond wake instability thresholds.

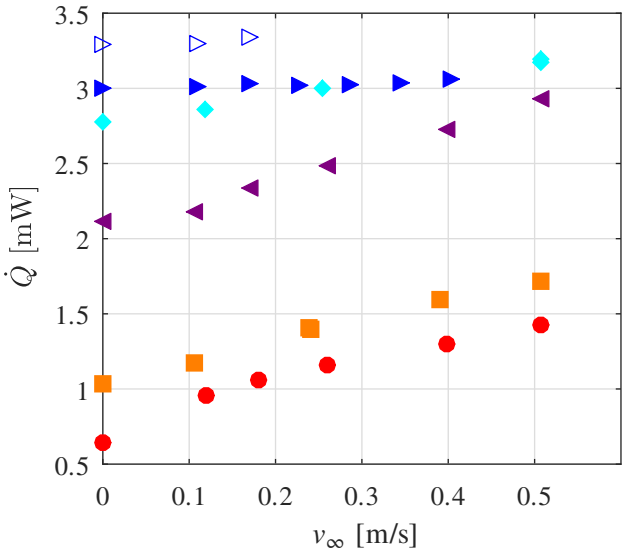


FIG. 5. Electrical power required to regulate at 25 K the wire heater as a function of the flow mean velocity for various bath temperatures: ● 2.28 K (0% superfluid), ■ 2.13 K (10% superfluid), ◀ 2.05 K (31% superfluid), ♦ 1.93 K (51% superfluid), ▶ 1.74 K (71% superfluid) in the "less conductive" regime, see Sec. IV), ▷ 1.74 K (71% superfluid) in the "more conductive" regime. Solid lines indicate the best linear fit for each data series.

Figure 5 presents the electrical power required to regulate the wire heater at 25 K versus the mean velocity, for flow temperatures ranging between 1.74 K (71% superfluid fraction) and 2.28 K (0% superfluid fraction). It shows that when the heater is submerged into an external flow, an additional electrical power is required to maintain its temperature. This conclusion is consistent with the previous observation in a jet flow [6] but we can now resolve more precisely the bath temperature dependence of $\dot{Q}$.

In two-dimensional laminar flows (such as, e.g., the flow around a thin wire) of classical fluids, at high Péclet numbers $\mathrm{Pe} = \mathrm{Re}\cdot\mathrm{Pr}$, where $\mathrm{Pr} = \nu/D \gg 1$ is the Prandtl number, with $D$ being the fluid thermal diffusivity, the heat transfer rate between a solid surface, and the fluid scales as $v_\infty^{1/2}$. This follows from the analysis [26, 27] of the convective-diffusive heat transfer in the thermal boundary layer. For the forced heat transfer around a heated wire this scaling has been experimentally and empirically confirmed in, e.g., Ref. [28]. In Fig. 6 we

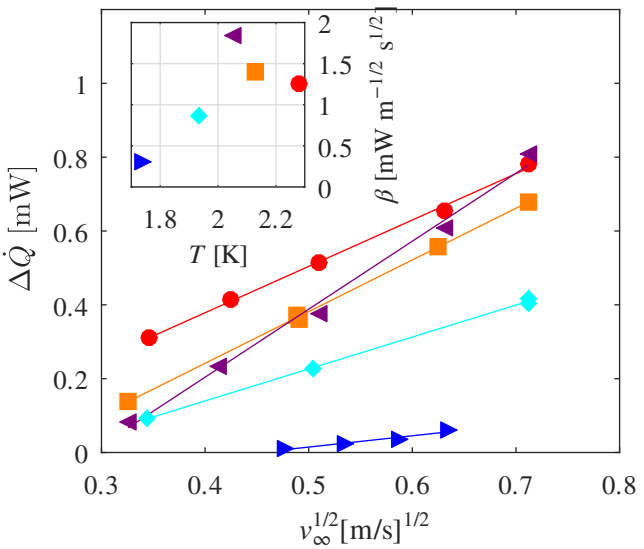


FIG. 6. Time average of the excess power required to overheat the wire at 25 K once the flow is turned on versus the square root of the velocity for various bath temperatures: • 2.28 K, ■ 2.13 K, ◀ 2.05 K, ♦ 1.93 K, ▶ 1.74 K in the "less conductive" regime (see Sec. IV). The markers indicate the actual computed values while the lines show the best linear fit of the data corresponding to Eq. (3). Inset: values of the slopes $\beta$ for all temperatures.

thus present the excess power

$$\Delta\dot{Q}(T_\infty, v_\infty) = \dot{Q}(T_\infty, v_\infty) - \dot{Q}(T_\infty, 0) \qquad (2)$$

required to maintain the temperature of the wire at 25 K once the flow is turned on, as a function of the square root of the velocity.

The best fit of the form

$$\dot{Q}(T_\infty, v_\infty) = \zeta(T_\infty) + \beta(T_\infty) \cdot v_\infty^{1/2} \qquad (3)$$

is calculated omitting the data at null velocity as is customary in standard fluids where natural convection prevents the $v^{1/2}$ scaling to hold down to small velocities. The coefficients $\zeta$ and $\beta$ are reported in Table II.

For completeness, we also reported in Table II the coefficients for a linear fit of the form

$$\dot{Q}(T_\infty, v_\infty) = \chi(T_\infty) + \gamma(T_\infty) v_\infty. \qquad (4)$$

where $\chi$ and $\gamma$ are temperature-dependent coefficients.

Due to the limited range of velocities, the above fits do not allow us to determine which of the two scaling laws, (3) or (4), is the best suited. At 2.28 K, in He I, we know from experience the $v^{1/2}$ scaling is better suited, and this probably remains true at 2.13 K, but at all other temperatures both laws could work.

A notable result, highlighted in the inset of Fig. 6, is the nonmonotonic dependence of the sensitivity to velocity versus the superfluid fraction (or fluid temperature $T_\infty$) with a maximum sensitivity somewhere between superfluid fraction of 10% and 50%; also note that the sensitivity to velocity significantly decreases for large superfluid fractions.

One point is worth stressing for subsequent modeling. For flow temperatures $T_\infty \geqslant 1.93$ K, the sensitivity to velocity, say defined as $d\dot{Q}/dv_\infty$, varies only slightly with the temperature, while $\dot{Q}$ significantly depends on it. In particular, the sensitivity in high temperature He II is close to sensitivity in He I, that is in the absence of superfluid.

| $T_\infty$ [K] | 2.28 | 2.13 | 2.05 | 1.93 | 1.74 |
|---|---|---|---|---|---|
| $X_{xf}$[%] | 0 | 10 | 31 | 51 | 71 |
| $\dot{Q}(v_\infty = 0)$ [mW] | 0.64 | 1.03 | 2.12 | 2.78 | 3.00 |
| $\dot{Q} = \chi + \gamma \cdot v_\infty$ | | | | | |
| $\chi$ [mW] | 0.74 | 1.05 | 2.06 | 2.78 | 3.00 |
| $\gamma$ [mW m$^{-1}$ s] | 1.45 | 1.37 | 1.68 | 0.81 | 0.12 |
| $\dot{Q} = \zeta + \beta \cdot v_\infty^{1/2}$ | | | | | |
| $\zeta$ [mW] | 0.52 | 0.71 | 1.59 | 2.57 | 2.86 |
| $\beta$ [mW m$^{-1/2}$s$^{1/2}$] | 1.26 | 1.40 | 1.84 | 0.87 | 0.30 |

TABLE II. Summary of the parameters obtained when fitting the power $\dot{Q}$ against $v_\infty$ (see Fig. 5) or $v_\infty^{1/2}$. The wire heater is overheated at constant temperature, here 25 K.

The sensitivity to velocity versus the wire heater temperature was not explored, but the experiment with the chip heater indicates that it can be significant (see e.g. Fig. 4).

## VI. HIGH FREQUENCY PEAK: THE COOLING GLITCHES

We now report a puzzling feature of heat transfer in a quantum flow: A well defined spectral peak in the PSD which we show can be attributed to the quasiperiodic occurrence of intense short-lived heat flux enhancements. These events have been named "cooling glitches".

### A. Emergence of a spectral peak

The wire heater was inserted in the grid flow and its temperature was maintained around 25 K. The time series of the electrical current has been analyzed.

Figure 7 shows the power spectral density (PSD) $\mathcal{P}(f)$ of the current in the wire for a superfluid fraction varied from 0% (2.28 K) up to 71% (1.74 K) and at a mean velocity $v_\infty = 0.250 \pm 0.015$ m/s.

In the absence of superfluid, the measured spectrum in the range of intermediate frequencies is compatible with the Kolmogorov spectrum of classical turbulence, as expected for grid turbulence (see Appendix for further discussion). For a 10% superfluid fraction ($T_\infty = 2.13$ K), the spectrum departs from the Kolmogorov shape above $\approx$ 500 Hz. For superfluid fractions equal to or larger

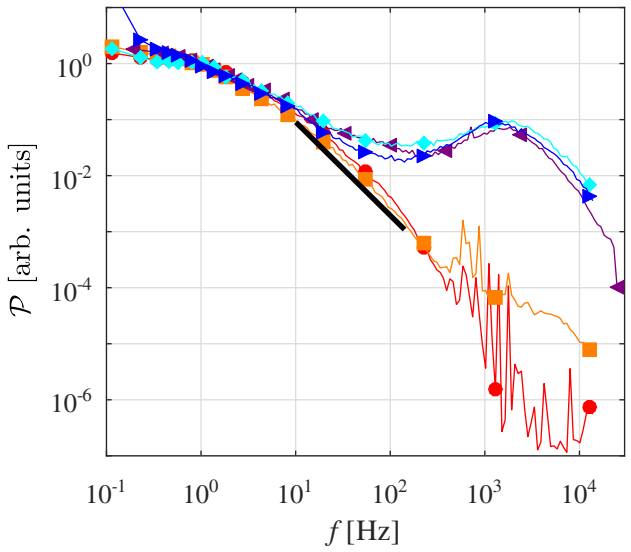


FIG. 7. Power spectral density $\mathcal{P}(f)$ of the current in the wire at 25 K for various flow temperatures: ● 2.28 K (0% superfluid), ■ 2.13 K (10% superfluid), ◀ 2.05 K (31% superfluid), ◆ 1.93 K (51% superfluid), ▶ 1.74 K (71% superfluid) in the "less conductive" regime (see Sec. IV). The black line shows a $f^{-5/3}$ power law. In each case, the mean velocity is $0.250 \pm 0.015$ m/s. The amplitude of the signal is rescaled so that spectra overlap at $f = 1$ Hz.

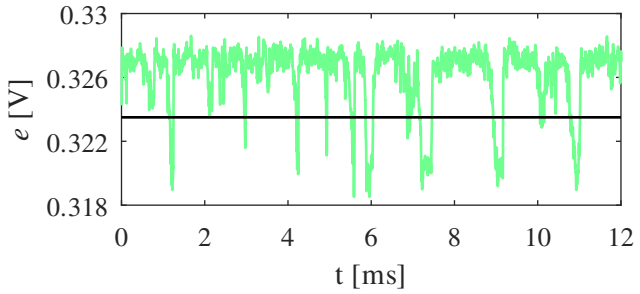


FIG. 8. Sample of the film heater voltage at $T_\infty = 2$ K as a function of time, with a mean fluid velocity $v_\infty \approx 0.38$ m/s as a function of time. The black horizontal line marks the chosen threshold.

than 31% ($T_\infty \leqslant 2.05$ K), a broad spectral bump centered around $f_p \approx 1$ kHz is observed. The bump is energetic enough to contribute to most of the variance of the signal.

A departure from the classical turbulence spectra has been previously reported using a similar heated wire in a superfluid jet experiment (see Fig. 2 in Ref. [6]), but the effect was much less pronounced and no peak reported. A possible explanation for not resolving a peak in this previous experiment is the combined effect of insufficient time resolution (the maximum resolved spectral frequency was 5 kHz) and faster time scales of the jet flow. Indeed, compared to the conditions of Fig. 7, the flow mean velocity was five times larger and the variance of velocity fluctuations $48^2$ times larger (peak excluded), which could shift a possible peak beyond the maximum resolved frequency.

### B. Evidences of cooling glitches

To gain more insight into the physical parameters that drive the high frequency behavior, an additional experiment was done using the film heater described in Sec. III C 2. This heater was operated in the grid flow at 2.0 K, but unfortunately it broke very rapidly so we only have one velocity condition, $v_\infty = 0.38$ m/s.

Figure 8 shows a small portion of the signal from the film heater. The heat transfer is enhanced during seemingly random brief periods, lasting typically a tenth of a millisecond or less.

The recorded time series for this smaller heater evidences the same spectral peaking at high frequency as illustrated by Fig. 9(a) which displays the PSD, $\mathcal{P}(f)$, from this film heater together with that from the wire at the same velocity but lower temperature (1.74 K). The bumps, even though they do not have the exact same shapes for the film and the wire, are located at nearby frequencies. This rules out the length of the heaters as a parameter governing the apparition of the bump since they have very different length (by two orders of magnitude). This also lets us assert that the electronic driving mode is not at fault: Whether the heater is driven at constant temperature (wire) or constant current (film), the bump remains.

Figure 9(b) shows the centered and normalized probability density function (hereafter PDF) of the output signal recorded from the wire and the film electronic drivers.

A first observation is that the PDF of the signals are skewed in opposite directions: The wire shows large excursions towards high current (positive skew $s \approx 0.83$), while the film shows large excursions towards low voltage (negative skew $s \approx -2.0$). These skewed PDF evidence that both heaters record rare and intense heat-flux events. The opposite signs of the skewness are easily explained by the difference in electronic drivers: The wire heater is driven at constant temperature while the film is driven at constant current. An increase of the cooling efficiency increases the current in the wire, but decreases the temperature of the film, and thus the measured voltage drop across it. Thus, both PDF indicate the existence of rare and intense events of enhanced heat transfer between the heaters and the flow. In the following, these events will be nicknamed "cooling glitches".

The dashed lines in Fig. 9(a) and Fig. 9(b) show respectively the PSDs and the PDFs of the same signals after a low-pass filtering at 400 Hz. As can be seen in Fig. 9(a), the result of the filtering is the suppression of the spectral bump, while in Fig. 9(b) we can see that each PDF becomes almost gaussian. To be precise, both PDFs end up with a small negative skew of order $s \approx -3.10^{-3}$, as expected for standard hot-film and hot-wire anemometer

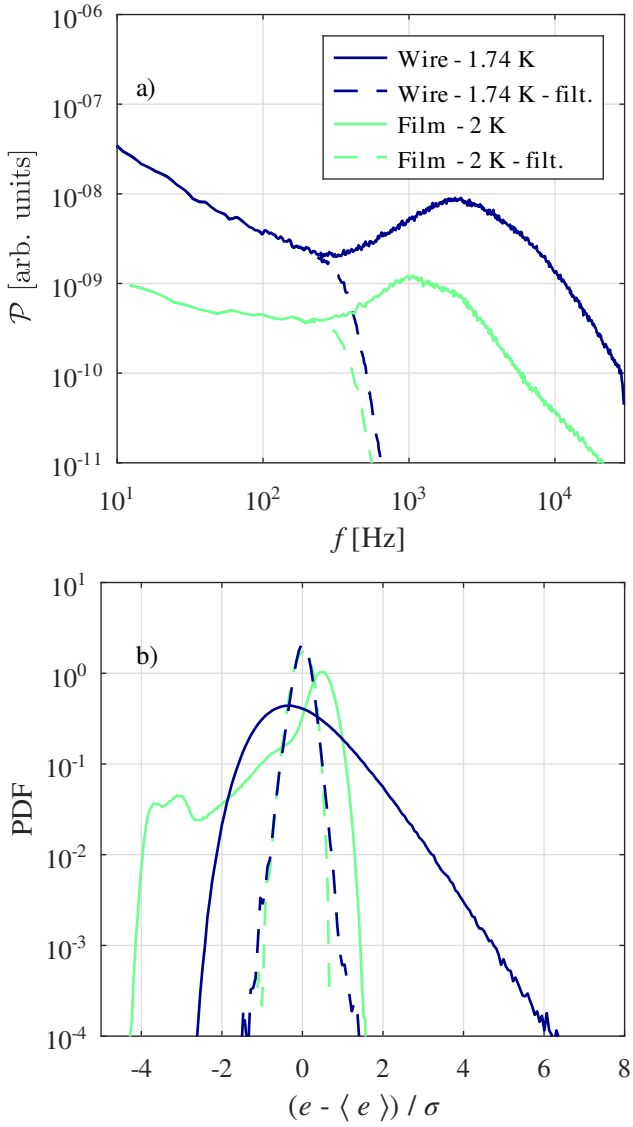


FIG. 9. a) Comparison of the PSD, $\mathcal{P}(f)$, of the film heater at $T_\infty = 2\,\mathrm{K}$ and of the wire heater at $T_\infty = 1.74\,\mathrm{K}$, , with a mean fluid velocity $v_\infty \approx 0.38\,\mathrm{m/s}$. Dashed lines correspond to the same data, but low-pass filtered at 400 Hz. b) Probability density function of the film and wire output signals in the same conditions as in a). The signals are centered and normalized by the standard deviations $\sigma$ of the unfiltered signals.

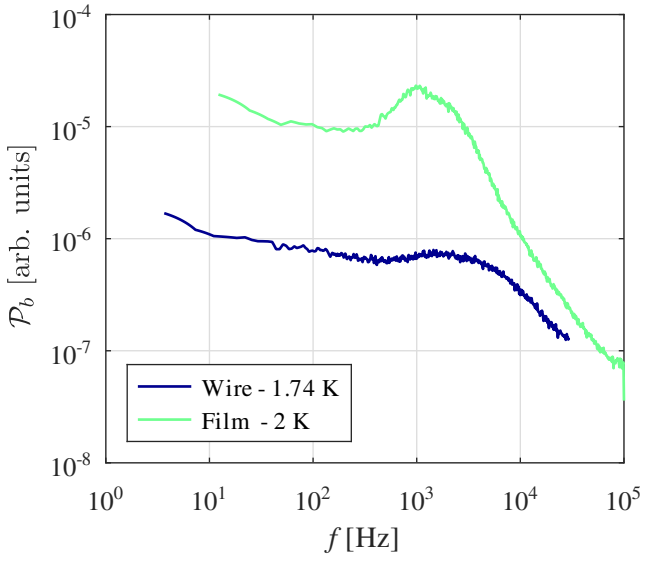


FIG. 10. Power spectral density $\mathcal{P}_b$ of the wire and film heaters binarized signals (see the text for detail).

in a turbulent flow of low turbulent intensity. Indeed, assuming that the PDF of the velocity is gaussian, the recorded PDF must be negatively skewed since the sensitivity to the velocity decreases with velocity. This filtering test strongly suggests that the cooling glitches, and the broad frequency peaks refer to the same phenomenon.

The bimodal shape of the film's PDF in Fig. 9(b) supports the view that the system is continuously switching between two well defined heat exchange modes: the default one, and one with a higher cooling efficiency.

In the time domain, the occurrence of a cooling glitch on the film heater can be spotted using an arbitrary threshold value, for instance the average between the peaks of both modes in the PDF ($e_{\mathrm{thresh}} \approx 0.3235V$, see the black line in Fig. 8. On the other hand, the PDF from the wire time series does not allow to resolve two distinct modes, possibly because of a lower temporal resolution. In order to binarize the wire heater signal we chose to define the threshold value as $e_{\mathrm{thresh}} = \langle e \rangle + 3\sigma$ where $\sigma$ is the standard deviation of the signal.

Figure 10 shows the PSD of the binarized signal, $\mathcal{P}_b(f)$, for both the film and the wire heaters. For the film, which has a clear bimodal behavior, the spectral bump is preserved and the frequency of its maximum is unchanged. The result is essentially the same for the wire except that the bump is much less pronounced than in the PSD of the raw signal.

The binarized signal only contains information about the temporal distribution of gliches, i.e. their duration and the time interval between them. The fact that this very basic signal has a spectral bump similar to that of the original signal, is another strong evidence that the glitches are the root cause of the spectral bump.

### C. Glitch characteristic frequency versus velocity

We have shown above that the sequence of cooling glitches exhibits a characteristic frequency scale of a few kHz in present flow conditions. We now characterize how this *glitch peak frequency* varies with the flow mean velocity.

The 1.74 K dataset from the wire is more specifically explored because it allows the most accurate quantitative assessments. Indeed, the sensitivity of the mean (and low frequency) signal to the velocity is the lowest and most

of the fluctuations of the energy of the signal are concentrated in the high frequency bump. At low velocity, we only used data acquired during a period of time where the wire was in the less conductive state since they prevail at most velocities (see Sec. IV).

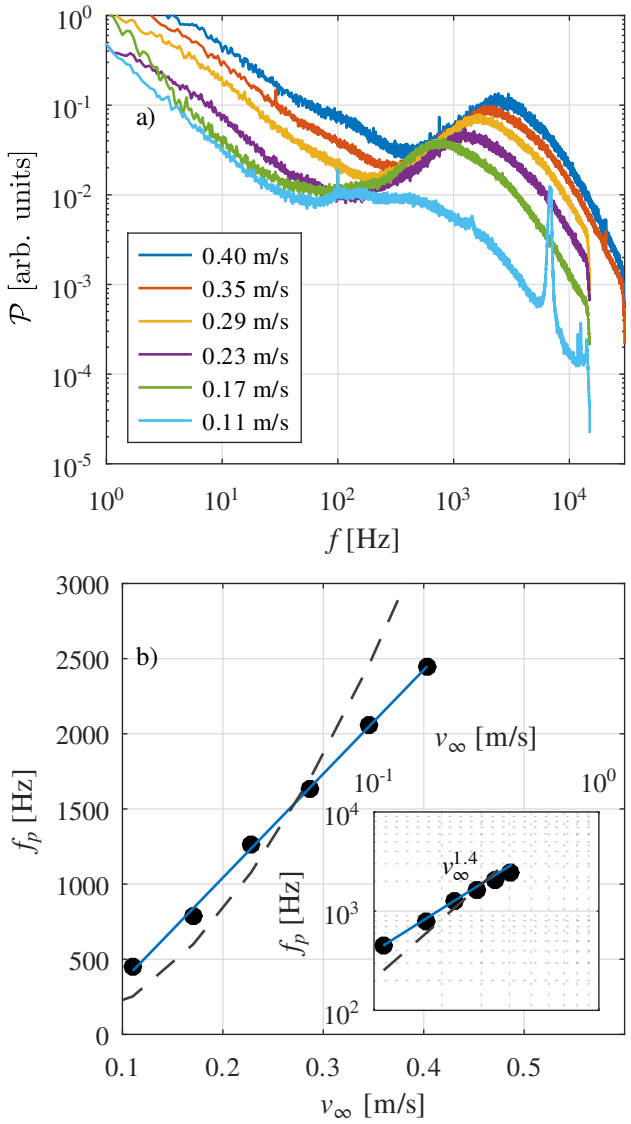


FIG. 11. a) PSD $\mathcal{P}(f)$ of the hot-wire voltage at 1.74 K for various flow velocities.
b) Frequency of the observed peak frequency as a function of the external flow average velocity (•), together with a linear fit (solid blue line) and the result of the model developed in the next section, see Eq. (43) (dashed line).
Inset: Same data in log-log coordinates. Here the solid line is a fit with a power law $f_p \propto v_\infty^{1.4}$.

Figure 11(a) shows the power spectra of the wire heater signal for various external flow velocities, and Fig. 11(b) the evolution of the peak frequency versus velocity. The peak frequency, extracted using a local third-order fit, is defined as the first local maximum above 500 Hz. Over the explored range, the velocity dependence of the peak frequency is consistent with an affine law $f_p = a + bv_\infty^\alpha$ with $\alpha \approx 1$, $a = -340\,\mathrm{Hz}$ and $b = 6912\,\mathrm{Hz\,s\,m^{-1}}$. This linear dependence suggests the existence of a fixed length scale in the flow of order $1/b \approx 150\,\mu$m, i.e. much larger than the wire diameter. The appearance of macroscopic length scales will be discussed in Sec. VII C.

On a log-log scale, the best power law fit of the data (see inset in Fig. 11(b)) is $f_p \sim v_\infty^\alpha$ with $\alpha \approx 1.4$. Obviously, the limited range of velocity -slightly more than half a decade- does not allow us to discriminate between both laws.

These scalings will be discussed in the next section.

## VII. DISCUSSION. MATHEMATICAL MODELING OF HEAT TRANSFER IN AN HE II EXTERNAL FLOW

### A. Analytical model of heat transport at zero velocity

At null velocity, Durì *et al.* [6] showed that the mean heat flux from a wire heater can be modeled satisfactorily assuming that a thin supercritical He I layer surrounds the wire and concentrates most of the temperature gradient. In this region, the temperature gradient $\boldsymbol{\nabla} T$ is proportional to the heat flux $\boldsymbol{\varphi}$, according to the standard Fourier law: the fluid temperature decreases from $T'_w$ in He at the surface of the wire ($r = r_w^+$), to $T_\lambda$ at $r = r_\lambda$. In the region $r > r_\lambda$ the temperature gradient evolves as [29–31]

$$\varphi^m = f(T)\frac{dT}{dr}, \tag{5}$$

where $f(T)$ is the so called conduction function; the power $m$ will be specified later.

This basic model, solved numerically, enabled us [6] to reasonably account for the mean heat transfer at all bath temperatures, including close to $T_\lambda$. In the following we solve the problem analytically.

Let $\dot{Q}$ be the heat rate needed to overheat the wire material at a mean temperature $T_w$ in a liquid helium bath at temperature $T_\infty$.

The problem is assumed to be axisymmetric and the aspect-ratio of the wire large enough to neglect ends effect. In such conditions, the wire temperature does not depend on the longitudinal coordinate and the heat flux around the heated wire is given by

$$\varphi = \frac{\dot{Q}}{2\pi l r} = \frac{\Phi}{r}, \tag{6}$$

where $l$ is the length of the wire and $r(\ll l)$ is the radial coordinate. Here the constant $\Phi$ is the heat transfer rate per radian and per unit length.

Let $T'_w$ be the temperature of helium in contact with the wire. Due to the thermal resistance within the wire

and Kapitza resistance at the solid-fluid interface, $T'_w < T_w$ and we can define a thermal resistivity $\rho_K$ such that

$$T_w - T'_w = \rho_K \Phi. \tag{7}$$

This temperature difference is expected to be more significant for the bulkier heaters (due to internal resistance), for nonmonolithic ones (due to internal interface resistance), and at lower overheating (due to larger Kapitza resistance at lower temperatures). For all reasons, this temperature drop is expected to be more relevant for the chip heater than for the wire heater. In the following, for simplicity, we will simply refer to this temperature drop as the "Kapitza correction".

In the supercritical He I region, the Fourier law writes

$$\frac{\Phi}{r} = -k\frac{dT}{dr}, \tag{8}$$

where $k$ is the thermal conductivity of helium. Neglecting the temperature dependence of $k$, the integration of Eq. (8) gives:

$$\Phi \ln\left(\frac{r_\lambda}{r_w}\right) = k(T'_w - T_\lambda). \tag{9}$$

In the superfluid He II region, Eq. (5) is integrated between $T_\lambda$ (at $r = r_\lambda$) and $T_\infty$ (for $r \gg r_\lambda$):

$$\frac{\Phi^m}{(m-1)r_\lambda^{m-1}} = \underbrace{\int_{T_\infty}^{T_\lambda} f(t)dT}_{F(T_\infty)}. \tag{10}$$

Here we have introduced the conduction integral $F(T_\infty)$. Eliminating $\Phi$ between Eqs. (9) and (10) we obtain

$$\ln\left(\frac{r_\lambda}{r_w}\right) = \frac{k(T'_w - T_\lambda)}{\left[(m-1)r_\lambda^{m-1}F(T_\infty)\right]^{1/m}}. \tag{11}$$

From the numerical solution [6] of this problem, we know that the width of the supercritical He I layer, is small compared with the radius of the wire (that is, $r_\lambda - r_w \ll r_w$), provided the bath temperature is not too close to $T_\lambda$ (say $T < 2.1$ K). As $\ln(r_\lambda/r_w) \approx (r_\lambda - r_w)/r_w \ll 1$, this necessarily requires that the right-hand side of Eq. (11) is small. Introducing a small parameter

$$\epsilon = \frac{k(T'_w - T_\lambda)}{\left[(m-1)r_w^{m-1}F(T_\infty)\right]^{1/m}} \ll 1, \tag{12}$$

and making use of the first-order asymptotic expansion of Eq. (10) with respect to $\epsilon$, we obtain for the heat rate per radian and unit length:

$$\Phi(T'_w, T_\infty) = \Phi_{II}(T_\infty)\left[1 + \epsilon\frac{m-1}{m} + O(\epsilon^2)\right], \tag{13}$$

where

$$\Phi_{II}(T_\infty) = \left[(m-1)r_w^{m-1}F(T_\infty)\right]^{1/m}. \tag{14}$$

From Eq. (11) it follows that the asymptotic expansion for $r_\lambda$, which determines the width, $r_\lambda - r_w$ of the supercritical layer, should be sought in the form

$$r_\lambda = r_w(1 + \epsilon + a_2\epsilon^2 + ...). \tag{15}$$

Making use of expansions (13) and (15), Eq. (9) can now be used to calculate the second-order term (i.e., the coefficient $a_2$) of the expansion (15). However, the second (and higher) order corrections are of no interest in the context of this work.

Neglecting the corrections of order $\epsilon^2$ and higher and making use of Eq. (12), which can be written as $\epsilon\Phi_{II} = k(T'_w - T_\lambda)$, it is more convenient to represent relation (13) in the form

$$\Phi(T'_w, T_\infty) \approx \Phi_I(T'_w) + \Phi_{II}(T_\infty), \tag{16}$$

where

$$\Phi_I(T'_w) = \frac{m-1}{m}k(T'_w - T_\lambda). \tag{17}$$

Here the heat flux per radian and per unit length appears as the sum of a contribution $\Phi_I(T'_w)$ due to the conduction in He I and a bath temperature-dependent contribution $\Phi_{II}(T_\infty)$ due to heat transport in He II. As $\epsilon \ll 1$, at low temperatures the former is much smaller than the latter. It is worth noting that such an additive contribution of heat fluxes is counterintuitive in thermal systems with resistances in series.

Making use of Eq. (7), Eq. (16) can be rewritten in terms of $T_w$ (instead of $T'_w$) and $T_\infty$: expression versus $T_w$:

$$\Phi(T_w, T_\infty) \approx \frac{1}{1+K}\left[\Phi_I(T_w) + \Phi_{II}(T_\infty)\right], \tag{18}$$

where

$$K = \rho_K\frac{m-1}{m}k \tag{19}$$

is a dimensionless parameter, later referred to as the Kapitza correction parameter which accounts for the strength of the temperature drop between solid and liquid.

Figure 12 presents the measured and the simulated values of the heat transfer rate $\Phi$ per unit length and radian as a function of temperature. We used the Bon-Mardion/Sato [29, 31] form of Eq. (5), with $m = 3.4$. The thermal conductivity of supercritical helium depends on temperature so we used its average value $k = 0.02\,\mathrm{W\,m^{-1}\,K^{-1}}$, determined using the HEPAK® library over the range 5 K – 25 K. Finally, the Kapitza correction was assumed negligible for the wire ($K \ll 1$). As can be seen, the above simple model yields reasonably good approximations for both absolute values and the temperature dependence, without any adjustable parameter. The

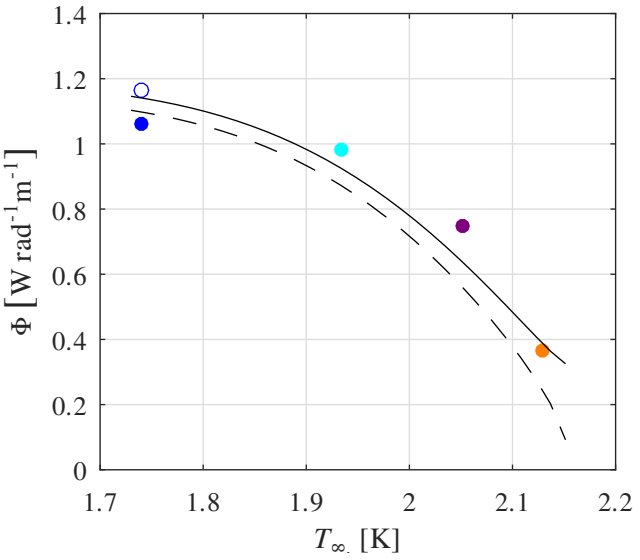


FIG. 12. Comparison of the measured and the modeled heat flux per radian and unit length (o). The solid line is the heat flux modeled according to Eq. (16), with no adjustable parameter, and the dashed line shows the exact numerical solution. Computations were done using $T_w = 25\,\mathrm{K}$.

contribution of the He I layer, $\Phi_I \approx 0.32\,\mathrm{W\,rad^{-1}m^{-1}}$, is about 28% the total heat flux at 1.74 K and 87% at 2.13 K.

We also solved Eq. (11) numerically to estimate $r_\lambda$ and then computed the exact value of the heat flux from Eq. (9) (see dashed line in Fig. 12). The relative error in the estimate of the total heat flux is about 4% at 1.74 K and 40% at 2.13 K. As expected, below 2.1 K the linear approximation $r_\lambda = r_w(1+\epsilon)$ [see Eq. (15)] is quite reasonable.

### B. Analytical model of heat transport at finite velocity

We now use an empirical approach to extend this analytical model and account for the extra heat transfer observed in the presence of the external flow.

The occurrence of one cooling glitch results in an increase of heat transfer. Thus, in principle, the overall velocity dependence of heat transfer could result from or be significantly affected by a change in the statistics of occurrence of glitches or a change in their strength. Still, this possibility could be discarded by the analysis of the histograms of instantaneous heat transfer. Indeed, they reveal that the most probable instantaneous heat transfer, which does not coincide with the occurrence of a glitch, has nearly the same velocity dependence as the mean heat transfer, glitches included.

As pointed out earlier, the sensitivity to velocity, say $d\Phi/dv_\infty$ varies only slightly with the flow temperature within the interval $1.93\,\mathrm{K} \leqslant T_\infty \leqslant 2.28\,\mathrm{K}$, although $\Phi$, or, more precisely, $\Phi_{II}$ vary significantly. The (chip) heater, sensitive to temperature near $T_\lambda$, has revealed that the velocity dependence is bound to the presence of a He I layer. The velocity dependence will thus be modeled by a modification $\Phi_I^\star(T_w', T_\infty, v_\infty)$ of the contribution $\Phi_I(T_w')$, so that

$$\Phi(T_w, T_\infty, v_\infty) = \Phi_I^\star(T_w', T_\infty, v_\infty) + \Phi_{II}(T_\infty). \qquad (20)$$

As customary in classical flows, the velocity dependence can be formally embedded in the Nusselt number $\mathrm{Nu}^\star(T_w, T_\infty, v_\infty)$ defined by the relation

$$\Phi_I^\star(T_w, T_\infty, v_\infty) = \mathrm{Nu}^\star \cdot \Phi_I(T_w'). \qquad (21)$$

This definition of $\mathrm{Nu}^\star$ is related to the classical Nusselt number Nu of the heat transfer from an arbitrary bluff body: $\mathrm{Nu}^\star(\mathrm{Re}) = \mathrm{Nu}(\mathrm{Re})/\mathrm{Nu}(0)$.

As discussed above in Sec. V [see Fig. 6 and Eq. (3) in particular], the heat transfer rate is consistent with a $v_\infty^{1/2}$ scaling with velocity, provided the magnitude of the velocity is sufficiently away from $v_\infty = 0$. We, therefore, will adopt the following model for the Nusselt number:

$$\mathrm{Nu}^\star = A + B\mathrm{Re}_w^{1/2}, \qquad (22)$$

where $A$ and $B$ are dimensionless constants of the order unity and $\mathrm{Re}_w$ is a Reynolds number based on the diameter of the wire [the definition is given below, see Eq. (23)].

In classical hydrodynamics, Eq. (22) is known as King's law and accounts for forced heat transfer from hot-wire anemometers (see e.g. Ref. [28]). The square root dependence is understood as the signature of the thermal boundary layer around the anemometer.

The reason why $\mathrm{Nu}^\star(\mathrm{Re}_w = 0) = A \neq 1$ reflects the existence of an alternative heat transfer mechanisms at zero velocity, e.g. natural convection.

Helium at 2.28 K is a classical fluid, and our wire heater resembles a hot-wire anemometer. Hence, it is not surprising that Eq. (22) accounts for heat transfer measurement above the superfluid transition at $T = T_\lambda$. The persisting agreement of Eq. (22) in a superfluid bath strongly suggests that a similar phenomenology remains at play, in particular the stretching of the He I layer surrounding the heater by the incoming flow.

Thus, for $T < T_\lambda$ the Reynolds number $\mathrm{Re}_w$ is defined as

$$\mathrm{Re}_w = \frac{d_w V_{\mathrm{eff}}}{\nu}, \qquad (23)$$

where $\nu$ is the kinematic viscosity of the He I layer surrounding the wire, and $V_{\mathrm{eff}} = (\rho_n v_n + \rho_s v_s)/\rho$ is the momentum velocity impinging on the He I thermal layer, resulting from the interaction between the external co-flow at velocity $v_\infty$ and the local counter-flow generated by the heater.

In the King's law, for classical fluids a Prandtl number correction $\mathrm{Pr}^{1/3}$ is sometimes included in the second term

of Eq. (22), but since this fluid's property is close to unity for helium in the range of pressures and temperatures of interest, this correction is not included in our simplified model.

From Eqs. (20), (21), and (22) it follows that the heat flux at arbitrary (subsonic) velocity can now be written as

$$\Phi(T_w, T_\infty, v_\infty) \approx \frac{1}{1 + K\mathrm{Nu}^\star} \left[\mathrm{Nu}^\star \Phi_I(T_w) + \Phi_{II}(T_\infty)\right]. \tag{24}$$

The velocity dependence is better evidenced by subtracting the heat flux $\Phi$ in the zero velocity limit $v_\infty \to 0^+$. Retaining the first-order Kapitza correction, we obtain

$$\begin{aligned}\Delta\Phi &= \Phi(T_w, T_\infty, v_\infty) - \Phi(T_w, T_\infty, 0^+) \\ &\approx B\mathrm{Re}_w^{1/2} \left\{\Phi_I - K\left[(2A + B\mathrm{Re}_w^{1/2})\Phi_I + \Phi_{II}\right]\right\}.\end{aligned} \tag{25}$$

At low enough velocity or temperature (e.g. below $\sim 0.1\,\mathrm{m/s}$ or below $\sim 2\,\mathrm{K}$, respectively), $\Phi_{II}$ is significantly larger than $\Phi_I^\star$, and Eq. (25) can be further simplified to obtain

$$\Delta\Phi \approx B\mathrm{Re}_w^{1/2} \left[\Phi_I(T_w) - K\Phi_{II}(T_\infty)\right]. \tag{26}$$

Having assumed that the effective velocity $V_{\mathrm{eff}}$ perceived by the He I layer surrounding the wire heater is proportional to $v_\infty$, we recover the expected $v_\infty^{1/2}$ dependence of heat transfer rate.

In Eq. (26), the term within square brackets increases monotonically with $T_\infty$. Therefore, the behavior with temperature of this term alone cannot explain the observed nonmonotonic dependence of the sensitivity to velocity [see $\beta(T_\infty)$ in the inset of Fig. 6]. The temperature dependence of the effective velocity impinging on the wire $V_{\mathrm{eff}}(v_\infty, T_\infty)$ must therefore contribute to this dependence, but this remains to be understood.

### C. Local heating in a co-flow and wing bluff bodies

This section addresses the flow patterns forming around the heater. We show that the flow on a heating wire resembles the flows on a symmetrical wing: on its leading edge for the normal-fluid, and its trailing edge for the superfluid. Each *virtual wing* is characterized by the two thickness length scales, respectively $L_n$ and $L_s = L_n\rho_n/\rho_s$, that are significantly larger that the wire diameter in our experimental conditions.

As a first step, the flows of the normal and superfluid components around a wire are modeled as two-dimensional potential flows in the plane perpendicular to the wire, the latter modeled as an infinitely long cylinder of radius $r_w$. The velocity potential $\Psi(r,\theta)$ of the flow around a cylinder is well known (see e.g. Ref. [32]):

$$\Psi(r,\theta) = v_\infty \cdot r\left(1 + \frac{r_w^2}{r^2}\right)\cos\theta, \tag{27}$$

where $r$ and $\theta$ are polar coordinates whose origin coincides with the axis of the cylindrical wire, and where the flow far from the origin is uniform along the $x$-direction with velocity $v_\infty$. This velocity potential accounts for the flows of both the normal and superfluid components of the external co-flow. A radial local counter-flow from a heating wire can also be described by the normal and superfluid velocity potentials $\Psi_n$ and $\Psi_s$:

$$\begin{aligned}\Psi_n(r,\theta) &= \frac{\Phi}{\rho S T}\ln\frac{r}{r_w}, \\ \Psi_s(r,\theta) &= -\frac{\rho_n}{\rho_s}\Psi_n(r,\theta).\end{aligned} \tag{28}$$

An analytical description of the normal and superfluid velocity fields ($\mathbf{v}_n$ and $\mathbf{v}_s$, respectively) is then obtained by superpositions of the local counter-flow potentials (28) with the co-flow potential (27): $\mathbf{v}_n = \boldsymbol{\nabla}(\Psi + \Psi_n)$ and $\mathbf{v}_s = \boldsymbol{\nabla}(\Psi + \Psi_s)$.

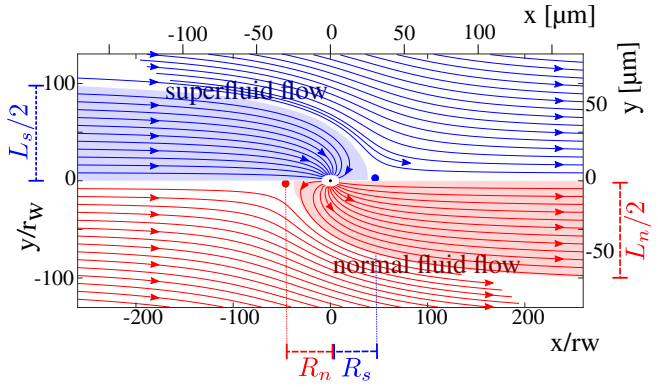


FIG. 13. Streamlines of the two-dimensional, normal, and superfluid potential flows around a cylinder of radius $r_w = 650\,\mathrm{nm}$ acting as a sink for superfluid (in blue, top half) and a source for the normal fluid (in red, bottom half). Each flow is symmetrical with respect to the axis $y = 0$. The velocity far from the cylinder is $v_\infty = 0.25\,\mathrm{m/s}$, and the sink/source properties match the local counter-flow produced experimentally for a superfluid fraction of 51% ($T_\infty = 1.93\,\mathrm{K}$) with $2\pi\Phi = 8.5\,\mathrm{W/m}$, which corresponds to a wire overheating around $T_w = 25\,\mathrm{K}$. The dimensionless and dimensional scales on both $x$ and $y$ axes are relevant for both fluids.

Figure 13 illustrates the streamlines of the superfluid (in blue, upper half of the panel) and normal fluid (in red, lower half) obtained from this model after matching the cylinder's radius and the mass-flow at the boundaries with the experimental conditions: a radius $r_w = 650\,\mathrm{nm}$, a co-flow external velocity $v_\infty = 0.25\,\mathrm{m/s}$, a superfluid fraction of 51% ($T_\infty = 1.93\,\mathrm{K}$), a heating rate per unit length $2\pi\Phi = 8.5\,\mathrm{W/m}$ (corresponding to the wire overheating $T_w \approx 25\,\mathrm{K}$). The background color highlights the flow regions with streamlines ending or starting at the surface of the heater.

The length scales of the normal and superfluid flow patterns, $L_n$ and $L_s$, respectively, are about two decades larger than the wire's radius ($L_n \approx L_s \approx 143\,\mu\mathrm{m}$, see

figure). Henceforth $L_n$ and $L_s$ are called the heater outer-flow scales.

On the (bottom) normal-fluid side of Fig. 13, the streamlines can be separated into those that are sourced by the heater, in the red background region, and the others. The first ones are within the flow "tail" of transverse length scale $L_n$ at $x = \infty$ (see Figure), which can be calculated from the thermal energy balance $L_n v_\infty \rho S T = 2\pi\Phi$, where $S$ is the specific entropy of the fluid, that is:

$$L_n = \frac{2\pi\Phi}{\rho S T v_\infty}. \tag{29}$$

A normal-fluid stagnation point forms upstream from the wire, at a distance $R_n$ calculated from the condition $v_n(r,\theta) = 0$ for $r = R_n$ and $\theta = \pi$:

$$\frac{\Phi}{\rho S T R_n} = v_\infty \left(1 - \frac{r_w^2}{R_n^2}\right) \approx v_\infty, \tag{30}$$

that is:

$$R_n \approx \frac{\Phi}{\rho S T v_\infty} = \frac{L_n}{2\pi}. \tag{31}$$

The flow of normal fluid outside the red region experiences a deflection similar to the one on the leading edge of a free-slip symmetrical wing of thickness $L_n$.

The blue background region on the (top) superfluid side of Fig. 13 shows streamlines "absorbed" by the heater surface. The superfluid flow outside this region experiences a sort of smooth backward step that resembles the flow in the vicinity of the trailing edge of a free-slip symmetrical wing. The thickness $L_s$ of this "superfluid wing" can be calculated from the mass conservation to yield

$$L_s = \frac{\rho_n}{\rho_s} L_n, \tag{32}$$

and the position of the superfluid stagnation point, $R_s$, can be obtained by analogy with the case of the normal fluid as

$$R_s \approx \frac{\rho_n}{\rho_s} R_n = \frac{\rho_n}{\rho_s}\frac{L_n}{2\pi} = \frac{L_s}{2\pi}. \tag{33}$$

The simple model described in this subsection preserves the key features of the normal and superfluid flows in the wide range of conditions explored. Thus, Fig.14 illustrates the flow patterns around the heating wire of radius $r_w = 650\,\mathrm{nm}$ for $T_\infty = 1.74\,\mathrm{K}$. Note that in the considered example the length scales of hydrodynamics patterns, whose dependence on physical parameters is given by Eqs. (29) and (32), remain significantly larger than the heater radius.

### D. Beyond the model of potential flows

We address now the limits of validity of the potential flow model developed in the previous subsection and analyze the effects of compressibility, viscosity, mutual friction, and vorticity that have been ignored so far. We show that the model developed above in Sec. VII C leads, nevertheless, to robust predictions for the outer-flow patterns at distances from the heater of the order of or larger than $R_n$ and $R_s$. Henceforth the flow in the vicinity of the heater will be called the "near-wire flow".

First it is important to stress that a heater in He II acts as a sink of the superfluid component mass flow and source of normal component mass flow, regardless of the potential-flow modeling. Thus the existence of superfluid flow pattern, of typical thickness $L_s$ [see Eq. (32)], resembling the trailing-edge of a wing is expected to be a robust feature of the flow, irrespective of modeling. The existence of a wing-leading-edge pattern of typical thickness $L_n$ [given by Eq. (29)] is also a robust feature but we will argue in the next subsection that its downstream shape probably resembles more a wiggling tail than that represented by nearly straight streamlines. For a point heater, the concept can be generalized straightforwardly with virtual obstacles having the shapes of three-dimensional fuselages rather than two-dimensional wings.

*Incompressibility.* By definition of length scales $R_s$ and $R_n$, the velocities at such typical distances from the wire and beyond are of order $v_\infty$, which, in the conditions typical of the experiment described above in this paper, is always significantly smaller than the lowest values of the first and the second sound velocities in He II (respectively 244 m/s and 6.5 m/s at 3 bar and 2.13 K). Describing the flows by incompressible potential fields is therefore justified for the outer flow and partly for the near-wire region.

*Viscosity.* Potential flows are irrotational and thus the model developed in Sec. VII C is not expected to be valid in the wire boundary layer due to viscous friction of the normal fluid. Nevertheless, compared to inertial effects, viscous effects are no longer prevalent in the outer flow field far enough from the wire. For instance, the relative weakness of viscous effects at distance $L_n/2$ for the wire can be assessed from normal fluid Reynolds number $\mathrm{Re}_{L_n} = L_n v_\infty \rho_n/\mu$, where $\mu$ is the dynamic viscosity of He I. This Reynolds number reaches its smallest values at larger temperature, where it indeed satisfies the requirement $\mathrm{Re}_{L_n} \gg 1$ (e.g., we find $\mathrm{Re}_{L_n} \gtrsim 492$ for $T_\infty = 2.13\,\mathrm{K}$ and $2\pi\Phi \gtrsim 2\,\mathrm{W/m}$). Thus, the flow patterns can be estimated neglecting the normal fluid viscosity in the outer flow and partly in the near-wire region.

*Mutual coupling and vorticity.* The chosen velocity potentials $(\Psi + \Psi_n)$ and $(\Psi + \Psi_s)$ describe uncoupled superfluid and normal fluid. In reality, the presence of superfluid vortices in the flow is responsible for the mutual friction between the two fluids, and eventually a strong coupling of their velocity fluctuations at scales significantly larger than the typical distance between superfluid vortices [33]. Below we will discuss in turn the following three flow regions: the upstream region, the close vicinity of the wire, and the region downstream of the flow.

Upstream, the inter-vortex distance $\delta_{\text{co-flow}}$ in the

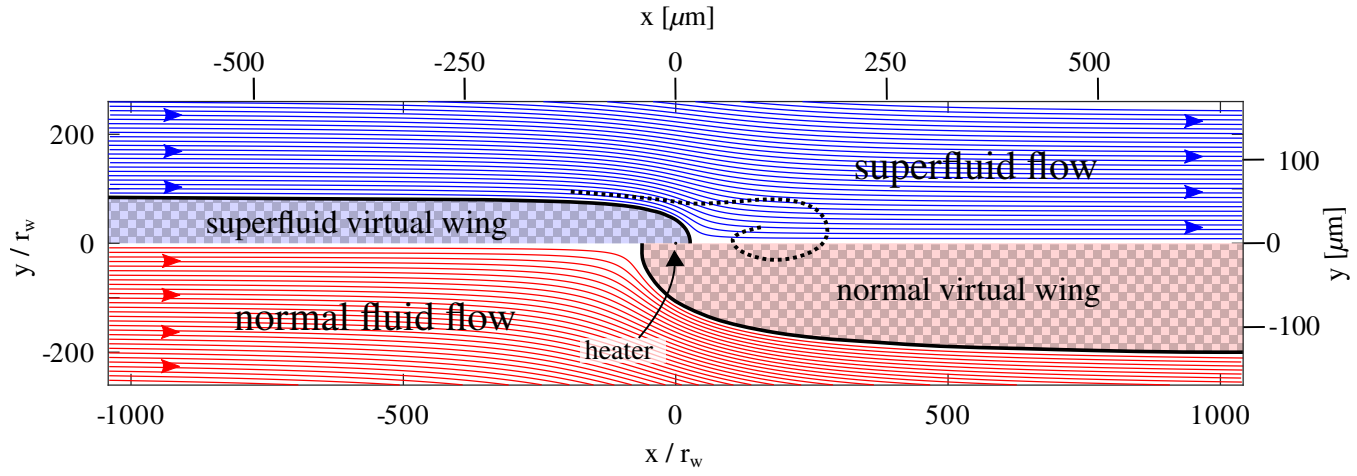


FIG. 14. Streamlines of the two-dimensional potential flows around a heater of radius $r_w = 650\,\mathrm{nm}$, for $v_\infty = 0.25\,\mathrm{m/s}$, a superfluid fraction of 71% ($T_\infty = 1.74\,\mathrm{K}$) and a heating rate $2\pi\Phi = 8.5\,\mathrm{W/m}$ ($T_w \approx 25\,\mathrm{K}$). The region of likely recirculation and instabilities is indicated with symbolic swirling streamlines. With superfluid-normal fluid coupling (not included here), the key hydrodynamic patterns (stagnation zones, contours of the virtual wings) are expected to be shifted and become time dependent, but we argue that their existence is a robust and generic consequence of the local heating in a co-flow.

weakly turbulent grid co-flow can be estimated from the turbulence intensity ($I \approx 2.6\%$, see Sec. III B), the turbulent integral length (say $L_f \approx 5\,\mathrm{mm}$), and the effective viscosity $\nu_{\mathrm{eff}}$ as

$$\delta_{\text{co-flow}} \approx \left(\frac{\nu_{\mathrm{eff}}\kappa^2 L_f}{I^3 v_\infty^3}\right)^{1/4} \approx 40\,\mu\mathrm{m}. \tag{34}$$

This formula has been validated by a number of studies [34–36]. The effective viscosity $\nu_{\mathrm{eff}}$ is an empirical quantity defined by postulating that $\epsilon = \nu_{\mathrm{eff}}\kappa^2\mathcal{L}^2$, where $\epsilon$ is the turbulence dissipation rate and $\mathcal{L}$ the average superfluid vortex line density [37]. In the considered range of temperatures, $\nu_{\mathrm{eff}}$ can be estimated from experimental values at saturated vapor pressure (see, e.g., Refs. [35, 37]) as $\nu_{\mathrm{eff}} \approx 10^{-8} - 10^{-7}\mathrm{m}^2/\mathrm{s}$, or just assuming for $\nu_{\mathrm{eff}}$ the value $\nu_{\mathrm{eff}} \approx \mu/\rho \approx 1.2\times10^{-8}\,\mathrm{m}^2/\mathrm{s}$ valid for the kinematic viscosity of the laminar He II flow, with the dynamic viscosity $\mu$ tabulated in Ref. [38], or, based on the model of Ref. [39], as $\nu_{\mathrm{eff}} \approx \rho_n B\kappa/(2\rho)$, where $B$ is a tabulated mutual friction coefficient of order unity [38]. Although those values can differ by one decade, they all lead to rather close estimates for $\delta_{\text{co-flow}}$ due to the 1/4 power law dependence in Eq. (34).

The order of magnitude of $\delta_{\text{co-flow}}$ is comparable to the characteristic scales of the outer-flow, which implies that the superfluid and the normal fluid are nearly uncoupled at such scales before entering the counter-flow region. Besides, the residual vorticity associated with the flow's turbulent background hardly distorts the streamlines due to the weak turbulence intensity. In this regard, the potential-flow picture is substantiated upstream from the heater.

In the wire's vicinity, the counter-flow velocities exceed the co-flow velocity $v_\infty$ and produce a dense turbulent tangle of superfluid vortices. The typical intervortex distances $\delta_{\text{ctr-flow}}$ within this tangle can be estimated from a well-known thermal counter-flow equation. Omitting an offset velocity, only relevant at low velocities, this equation can be written in the form

$$\delta_{\text{ctr-flow}}(r) = \frac{1}{\sqrt{a}|v_s(r) - v_n(r)|}, \tag{35}$$

where $\mathbf{v}_s \cdot \mathbf{v}_n < 0$ and $a(T)$ is a numerical coefficient tabulated in the literature (see e.g. Ref. [40]). Substituting the counter-flow velocities $v_n = \partial\Psi_n(r)/\partial r$ and $v_s = -v_n\rho_n/\rho_s$, one obtains

$$\delta_{\text{ctr-flow}}(r) = \frac{r}{L_n/2}\frac{\pi}{v_\infty\sqrt{a}(1+\rho_n/\rho_s)}. \tag{36}$$

The counter-flow velocities match in strength the external velocity $v_\infty$ typically at one outer-scale distances from the wire. Equation (36) is no longer strictly valid at such distance but it should still provide an order of magnitude estimate for the typical intervortex distance upstream from the heater or in the transverse direction. For instance, for the experimental conditions modeled in Fig.13 (1.93 K, 3 bars, and $v_\infty = 0.25\,\mathrm{m/s}$), we find

$$\delta_{\text{ctr-flow}}(L_n/2) \approx \delta_{\text{ctr-flow}}(L_s/2) \approx 1.4\,\mu\mathrm{m},$$

which is two decades smaller than $L_n \approx L_s \approx 140\,\mu\mathrm{m}$.

We now question if this tangle is dense enough to enforce a significant coupling between the superfluid and the normal fluid at the outer-flow scales $L_s$ and $L_n$. Owing to the large scale separation between $\delta_{\text{ctr-flow}}$ and $L_s, L_n$, the superfluid can be described as a continuous medium characterized by a local vortex line density $\delta_{\text{ctr-flow}}^{-2}$ and a coarse grained velocity $\widetilde{\mathbf{v}_s}$. In such conditions, the coupling between the superfluid and the normal

components can be described, as first approximation, by a volumetric mutual friction force whose magnitude, $F_{ns}$ can be written in the Görter-Mellink form

$$F_{ns} = \frac{\rho_n \rho_s}{\rho} \frac{B}{2} \kappa \delta_{\text{ctr-flow}}^{-2} |\mathbf{v}_n - \widetilde{\mathbf{v}_s}|.$$

Making use of the coarse-grained Hall-Vinen-Bekarevich-Khalatnikov equations (see e.g. Ref. [5]), it is straightforward to identify the relaxation times $\tau_n$ and $\tau_s$, due to the mutual friction force, for the normal and superfluid components, respectively, from the estimates for the material derivatives $|\rho_n D\mathbf{v}_n/Dt| \sim F_{ns}$ and $|\rho_s D\mathbf{v}_s/Dt| \sim F_{ns}$:

$$\tau_n(r) = \frac{\rho_n}{\rho_s} \tau_s(r) = \frac{2\rho}{B\kappa\rho_s} \delta_{\text{ctr-flow}}^2(r). \tag{37}$$

The superfluid coarse grained velocity $\widetilde{\mathbf{v}_s}$ at a distance $\sim L_s/2$ from the heater evolves with the characteristic time scale $L_s/(2v_\infty)$. The mutual coupling will alter significantly the normal fluid streamlines if the relaxation time $\tau_n(L_s/2)$ is short enough, say $\tau_n(L_s/2) \lesssim L_s/(2v_\infty)$. Similarly, mutual coupling will alter the (coarse-grained) superfluid streamlines at a distance of order $L_n/2$ if $\tau_s(L_n/2) \lesssim L_n/2v_\infty$. In the experimental conditions modeled in Fig. 13 (1.93 K, 3 bars, $v_\infty = 0.25\,\text{m/s}$, $B \approx 1$, $\rho \approx 2\rho_s \approx 2\rho_n$), both inequalities become identical and are found to be valid:

$$78\,\mu\text{s} \approx \frac{4}{B\kappa} \left[\delta_{\text{ctr-flow}} \left(\frac{L_s}{2}\right)\right]^2 \lesssim \frac{L_s}{2v_\infty} \approx 280\,\mu\text{s}.$$

More generally, using Eqs. (29), (32), (36), and (37), the criteria for partial fluid locking reduce to

$$\frac{2\pi\rho ST}{B\kappa a(T)} \frac{\rho_n}{\rho} \left[\max\left(1, \frac{\rho_s}{\rho_n}\right)\right]^2 \lesssim \Phi. \tag{38}$$

Interestingly, this locking condition amounts to comparing the heat flux with a quantity that depends only on the helium properties. To the best of our knowledge, the empirical, temperature-dependent coefficient $a(T)$ is not tabulated in pressurized helium but the full left-hand-side term can be estimated at saturated vapor pressure, and it is found to have roughly the same magnitude as the right-hand-side term of condition (38), $\Phi$ shown in Fig. 12.

This shows that the dense superfluid vortex tangle around the heater must strongly couple the superfluid and the normal components over length scales encompassing the outer-flow scales $L_s$ and $L_n$, an effect ignored in our simple velocity-potentials model. We thus expect some distortion of the streamlines, shown in Figs. 13 and 14 within a few $L_s$ and $L_n$ from the heater. Besides, the strong mutual coupling will favor a locking of the wakes of both fluids and allow vortical structures to develop in the wake of the heater, definitely invalidating the model of the irrotational, potential velocity fields downstream from the heater. The issue of the turbulent wake that forms downstream of the heater is addressed in the next subsection.

### E. The turbulent wake of the heater

In the previous subsection, we predicted two consequences of a localized heating in a quantum flow. First, the emergence of virtual obstacles of typical size $L_s \gg r_w$ (for the superfluid) and $L_n \gg r_w$ (for the normal fluid) across the flow. Second, a strong coupling of the superfluid and the normal component flows at length scales of the order and exceeding $\max(L_s, L_n)$; however, in the vicinity of the heater [say for $r \lesssim \max(L_s/2, L_n/2)$] the counter-flow velocities remain significant so that the two fluids tend to move in opposite directions.

Numerical simulations are probably needed to explore the resulting hydrodynamic patterns but this is beyond the scope of this study. Nevertheless, based on a few simple hypotheses we can assess the flow stability. First we assume that the outer-flow stability is controlled by a wake Reynolds number $\text{Re}_{\text{ctr-flow}}$. As the superfluid "wing trailing-edge" profile is possibly destabilized at distances of the order $L_s$ from the heater (symbolized by the curvy streamline of Fig. 14), we now define the Reynolds number $\text{Re}_{\text{ctr-flow}}$ of the flow based on the characteristic length $L_s$. As we lack a better understanding of the interplay between the superfluid and the normal fluid wakes, such a choice of the length scale to satisfy the conditions of stability is rather conservative ($\max(L_s, L_n)$ would be a less conservative choice; however, such a choice would not change our quantitative conclusions). At distances of the order $\max(L_n, L_s)$ in the wake of the wire, the counter-flow velocity is small compared to $v_\infty$ but the vortex tangle still remains dense, thus entailing some relocking of the superfluid and the normal fluid velocity fluctuations at scales larger than the intervortex distance. He II can then be described as a single fluid of density $\rho = \rho_s + \rho_n$ and velocity $v \approx v_s \approx v_n$ that inherits the viscous volumetric force of the normal fluid $\mu\nabla^2\mathbf{v}_n \approx \mu\nabla^2\mathbf{v}$. The kinematic viscosity $\nu = \mu/\rho$ of this fluid is thus a natural choice for the denominator of $\text{Re}_{\text{ctr-flow}}$. Hence, the wake Reynolds number defined to assess the stability of the outer-flow is

$$\text{Re}_{\text{ctr-flow}} = \frac{L_s v_\infty}{\mu/\rho} = \frac{\rho_n}{\rho_s} \frac{2\pi\Phi}{ST\mu}. \tag{39}$$

Interestingly, this Reynolds number depends only weakly, through $\Phi(v_\infty)$, on the velocity of the external co-flow, $v_\infty$. Formally, Eq. (39) reduces to a Reynolds number characterizing the counter-flow generated by the heater. It can be formally written using the wire diameter $2r_w$ as the characteristic length and a characteristic velocity proportional to the counter-flow superfluid velocity $v_s = \partial\Psi_s(r)/\partial r$ extrapolated at the surface of the

wire ($r = r_w$):

$$\mathrm{Re}_{\text{ctr-flow}} = \frac{(2r_w)[\pi v_s(r_w)]}{\mu/\rho}\,. \tag{40}$$

In present experimental conditions, $\mathrm{Re}_{\text{ctr-flow}}$ reaches a few thousands, far beyond the instability threshold of a flow behind standard bluff bodies, which becomes unsteady typically for Reynolds number of a few tens. To summarize, the heater is expected to generate a turbulent wake of the locked superfluid and the normal fluid and having a characteristic Reynolds number weakly dependent on the co-flow velocity $v_\infty$.

### F. The vortex street

In classical hydrodynamics, periodic large scale eddies can form in the wake of a bluff body [41]. These structures, sometimes called von Kármán vortex streets, are characterized by their shedding frequency $f = \mathrm{St}\cdot U/D$ where $U$ is the flow velocity, $D$ is a characteristic transverse size of the obstacle, and St is the Strouhal number [42] of the order 0.1 – 0.3 determined by the obstacle shape and the Reynolds number based on $U$ and $D$. In a turbulent flow, the periodicity of vortex shedding can be altered and its frequency is not well defined (see, e.g., Ref. [43]).

For a cylindrical obstacle of diameter $D$, $\mathrm{St} \approx 0.20 \pm 0.03$ over the range of Reynolds number $DU/\nu \approx 10^2 - 2\times 10^5$. For a symmetrical flat wing of thickness $D$ with semicircular leading and trailing edges, the Strouhal number is slightly larger, e.g., $\mathrm{St} \approx 0.27$ for the aspect ratio 10 and the Reynolds number of 1300 [44]. The latter geometry is not directly comparable to ours due to the absence of boundary layer along the superfluid virtual wing.

Since this vortex shedding effect is inertial and not viscous [45, 46], it is expected to exist in superfluids, although not observed yet to the best of our knowledge. Could a vortex street account for the spectral bump at frequency $f_p$ of the heat transfer measurement reported above in Sec. VI C? In other words, could cooling glitches be triggered by the shedding of vortices in the wake of the heater?

Qualitatively, the absence of the spectral bump at zero velocity is consistent with this hypothesis. The profile of typical individual cooling glitches, illustrated in Fig. 10(b), is also consistent with emergence of a non-classical boundary layer, attached to the heater (in the form of either the He I shell, or/and the superfluid vortex tangle around it), which undergoes a re-formation once the velocity perturbations are advected away.

More quantitatively, the vortex shedding frequency predicted by the Strouhal formula can be compared with the measured frequency of the "bump". $U = v_\infty$ is a natural choice for the characteristic velocity of the flow. For now, the effective transverse length scale of the bluff body will be denoted $D(T, v_\infty)$. The vortical patterns emitted behind a symmetrical bluff body have vorticity of alternating signs, and the frequency given by the Strouhal number corresponds to the frequency of emission of a vortex-antivortex pair. Both vortices from one pair can trigger a glitch so that their characteristic frequency $f_p$ would then be twice the Strouhal frequency, $f_p = 2\times \mathrm{St}U/D$. This leads to the following prediction for the frequency of the spectral bump:

$$f_p = \frac{2\mathrm{St}v_\infty}{D(T, v_\infty)}\,. \tag{41}$$

For numerical estimates, we arbitrarily take an intermediate Strouhal number between the two values cited above: $\mathrm{St} = 0.23$.

Measurements reported in Fig. 11(b) are consistent with a linear velocity dependence of $f_p(v_\infty)$, suggesting a weak velocity dependence of $D$. The spectra of Fig. 7 are consistent with a spectral bump frequency increasing by at most few tens of percents from 1.74 K to 2.05 K, suggesting also a weak temperature dependence of $D$ over this range. This leads to a preliminary estimate within $1.74\,\mathrm{K} - 2.05\,\mathrm{K}$ and $v_\infty < 0.4\,\mathrm{m/s}$:

$$D(T, v_\infty) \simeq 75\,\mu\mathrm{m}\,. \tag{42}$$

This length scale is significantly larger than the wire diameter. As shown in Sec. VI B, we can rule out other geometrical features of the wire, such as its length, since the spectral peaking above 1 kHz associated with this length scale is also observed with the geometrically dissimilar film probe. Moreover, we can reasonably exclude that a fixed length scale smaller than 100 microns is present in the incoming flow, since the smallest (nearly) velocity-independent flow scale is expected to be the integral scale, which is about two decades larger. We show below that a correct order of magnitude for $D$ can be obtained from the naive hypothesis that the thickness $L_s$ of the destabilizing trailing edge plays the role of the obstacle transverse length scale. Indeed, this leads to

$$f_p \sim \frac{2\mathrm{St}v_\infty}{L_s} = \frac{\mathrm{St}v_\infty^2}{\pi\Phi}\frac{\rho_s}{\rho_n}\rho S T\,. \tag{43}$$

This equation corresponds to the dashed line in Fig. 11(b). Strikingly, this naive estimate gives the correct order of magnitude for the frequency.

The nearly quadratic $f_p \sim v_\infty^2$ scaling [neglecting the $\Phi(v_\infty)$ dependence] contrasts with the apparent scalings $f_p \sim v_\infty$ or $f_p \sim v_\infty^{1.4}$ of experimental data [see Fig. 11(b) and its inset], indicating that this simple model does not fully account for the phenomenology at play. Two corrections could possibly reduce the disagreement. First, the hypothesis of a 2D flow is not accurate since the wire length (450 microns) is not much larger than $L_s$. The scaling of $L_s(v_\infty)$ could therefore slightly tends toward the scaling of the axi-symmetric thermal flows expected for point heaters, that is $L_s \sim v_\infty^{-1/2}$, which could

contribute to explain the sub-quadratic dependence of $f_p(v_\infty)$. Second, a measurement bias may also contribute to this apparent disagreement: an underestimate of the true experimental bump frequency at the largest velocities due to some spectral cut-off.

Over the range $1.74\,\mathrm{K} - 2.05\,\mathrm{K}$, Eq. (43) predicts a 38% decrease of $f_p$, not compatible with measurements. This suggests that a model for the effective length scale $D$ depending both on $L_s$ and $L_n$ would be more relevant [47].

Further experimental studies in the range $2.05\,\mathrm{K} - 2.13\,\mathrm{K}$ and numerical simulations would be interesting to complete and underpin this vortex shedding model.

### G. The peak as a filtered high frequency noise

We present here an alternative explanation of the observed spectral bump at high frequency.

Instead of characterizing the bump by the frequency of its maximum, as could have been justified by the resonant or instability mechanisms, the bump can *a-priori* be seen as the result of a competition between two opposite processes: a forcing emerging above some frequency $f_{\mathrm{left}} < f_p$ (left side of the bump) and a cut-off mechanism at higher frequencies (right side of the bump). For instance, the left-side of the bump could be linked to the onset of processes triggering the cooling glitches, and the right side to a cut-off associated with a recovery mechanism bounding the lowest time interval between glitches. It could also be associated with a finite response time of the heater material and/or the thermal boundary layer.

Figure 15 present spectra in semilogarithmic axis, with frequency on the $x$ axis compensated by some power of the mean velocity. On the $y$ axis, the power spectral density $\mathcal{P}(f)$ is multiplied by $f$ so that the surface under the "curve" is proportional to energy $E$ despite the use of logarithmic scale; indeed, for any frequency interval $\Delta f$ we have

$$E(\Delta f) = \int_{\Delta f} \mathcal{P} df \propto \int_{\Delta f} f\mathcal{P} d(\log_{10} f) \qquad (44)$$

In Fig. 15, the best collapse of the left (Fig. 15(a)) and right (Fig. 15(b)) hand sides of the bump on single curves is obtained by compensating the $x$ axis frequency by $v_\infty^\alpha$ with, respectively, $\alpha = 1.2 \pm 0.2$ and $\alpha = 0.5 \pm 0.05$.

As discussed previously, in the outer flow region the two components of He II are expected to become decoupled at scales proportional to the inter-vortex spacing, $\delta \propto v_\infty^{-3/4}$. Below this decoupling scale, it has been predicted that the kinetic energy of the superfluid component, cascading from larger length scales, will pile up, a phenomenon sometimes referred to as "bottlenecking" or a trend to equipartition [48]. At mesoscales this manifests itself as an enhancement of the superfluid velocity fluctuations. If, by some mechanism yet to be determined, the cooling glitches are triggered by those fluctuations, then we could expect the formation of the left side of the peak for frequencies that scale like $f_{\mathrm{left}} \propto v_\infty/\delta \propto v_\infty^{7/4}$.

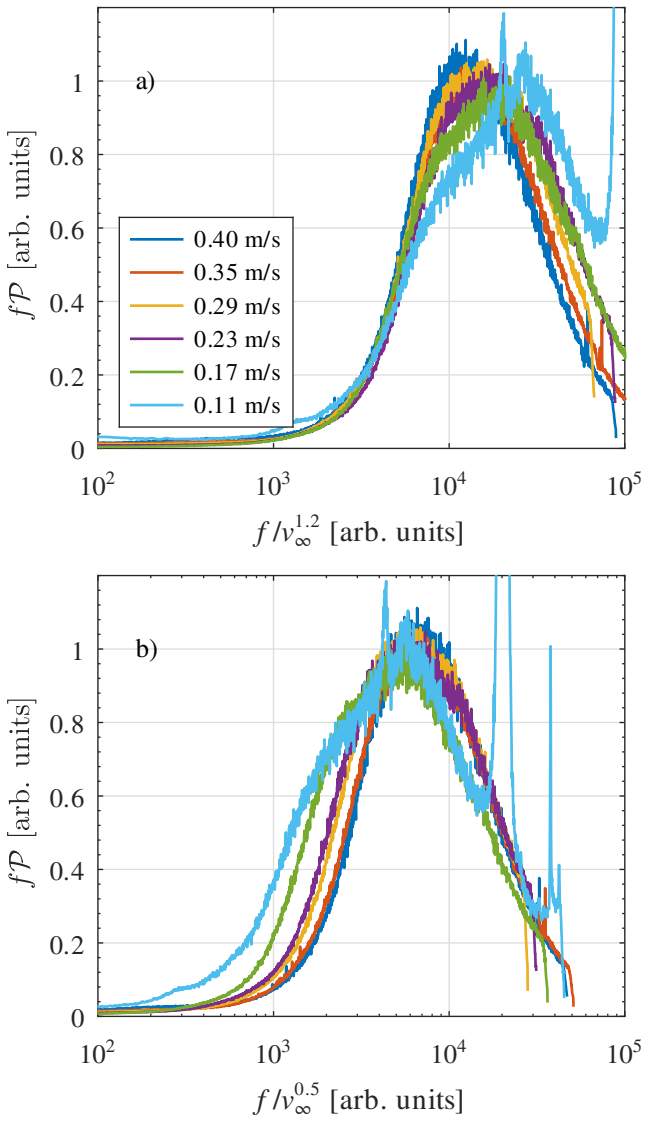


FIG. 15. Rescaled power spectral density $f\mathcal{P}(f)$ of the wire signal at 1.74 K for various external velocities as a function of the frequency compensated by $v_\infty^\alpha$ with $\alpha = 1.2$ (a) and $\alpha = 0.5$ (b). To better illustrate on the left and right single curves [panels (a) and (b), respectively] the amplitude of the rescaled PSD was normalized for all maxima.

As for the right part of the spectrum, the $v_\infty^{1/2}$ scaling could be associated with the thermal response time of the boundary layer: As the velocity increases, the He I thermal boundary layer thickness is expected to scale as $v_\infty^{-1/2}$, and so does the thermal response time. This yields a cut-off frequency $f_{\mathrm{right}} \propto v_\infty^{1/2}$.

## VIII. SUMMARY AND CONCLUDING REMARKS

Making use of miniature heaters, we have explored the forced heat transfer in a subsonic flow of superfluid helium at velocities up to 3 m/s. Our experimental results yield the following four main properties of the heat transfer in He II flows:

- In the case of a sufficiently large overheating of the heater, some velocity dependence of the heat transfer rate emerges when the fluid in contact with – and in the close vicinity of– the heater looses its superfluidity.
- Two metastable heat transfer regimes exist at large superfluid fraction and low velocity. As the velocity is increased, the state of lower conduction progressively supersedes the higher conduction state hence leading to a depletion of the mean heat transfer.
- Short-lived cooling enhancements, named *cooling glitches*, occur quasiperiodically with a velocity-dependent characteristic frequency $f_p$. Their signature in the spectral domain is a broad spectral peak.
- Heat transfer sensitivity to velocity reaches a maximum for a fluid temperature of $2.0 \pm 0.1$ K.

An analytical model is proposed to describe these observations. At zero velocity, it accounts quantitatively for the heat transfer, including its temperature dependence. At finite velocity, the velocity dependence is also accounted for, but the maximum, observed at temperatures around 2 K, of sensitivity of the heat transfer rate to velocity, remains yet unexplained, as well as the observation of metastable states at low velocity and low temperature.

A semiquantitative analysis of the flow around the wire heater is proposed, distinguishing the superfluid and normal fluid components of the quantum fluid. We predict the formation, around the heater, of flow patterns in the superfluid and the normal components whose characteristic scales, respectively $L_s$ and $L_n$, are two decades larger than the heater diameter in our experimental configuration. The superfluid (resp. normal fluid) pattern is reminiscent of the flow over the trailing (resp. leading) edge of a symmetrical wing. It is argued that the dense quantum vortex tangle sustained by the heater couples the superfluid and normal fluid patterns, resulting in the formation of a strongly turbulent wake with locked superfluid and normal fluid components.

The characteristic frequency $f_p$ revealed by heat transfer measurements is quantitatively consistent with the formation of a von Kármán vortex street in the wake of the heater. Still, a precise dependence on the velocity and temperature is not fully accounted for by the model, calling for further investigations on the relation between the effective transverse length scale of the obstacle and the size of the virtual wings $L_s$ and $L_n$. We thus discuss an alternative explanation for the appearance of a broad spectral peak (the so-called "bump") at some characteristic frequency $f_p$ in connection with an existing prediction of a piling up (or "bottlenecking") of the superfluid kinetic energy at small scales [34]. We argued that such a peak may result from the competition between instabilities (cooling glitches) triggered at frequencies above $f_{\text{left}} < f_p$ and a cut-off mechanism at higher frequencies.

Numerical studies are certainly needed to better understand the mutual coupling of the superfluid and normal components in the region of local counter-flow generated by the heater, and the relation between $L_n$, $L_s$, and the velocity $V_{\text{eff}}$ perceived by the He I boundary layer. For instance, it would be interesting to see if the resulting flow is controlled by the largest or smallest of the two scales $L_s$ and $L_n$, which could explain why the maximum sensitivity to velocity is reached near 2 K, that is when $L_s \approx L_n$.

To conclude, although the heat transfer mechanisms at play are not yet fully understood and deserve further investigations, two applications of the present study can already be suggested.

First, the miniature heater within the quantum flow can be seen as an obstacle with a tunable length scale. Indeed, the length scales $L_s$ and $L_n$ depend on the amount of heating and not on the external flow velocity. Hence, a three- or two-dimensional network of miniature heaters positioned across a flow can be seen as a bluff body with a remotely controllable shape. This opens an interesting perspective in the studies of turbulence generated by an active grid or an active wing.

Second, a successful operation of the hot wire anemometer in superfluid has been previously reported [6]. The present study confirms the analysis and conclusions of the cited work but also allows us to identify the following limitation of the hot-wire anemometry in a quantum flow: The space-time resolution is spoiled by the formation of the outer flow scales ($L_s$ and $L_n$) and the associated time scales ($L_s/v_\infty$ and $L_n/v_\infty$). In particular, the broad peak in the spectral response cannot be interpreted directly as a feature of the external flow, and it would be hazardous to identify it with the predicted bottlenecking of the velocity spectra in superfluid helium at finite temperature[34, 49].

## IX. ACKNOWLEDGMENTS

We thank Bernard Castaing for providing us with a key step allowing building the analytical expression for the heat transfer at null velocity. We also thank Rémi Benhafed and Jérome Chartier for support in designing an running the experiment. This work is supported by the European Commission – European High-performance Infrastructures in Turbulence (CEEuHIT, project "MOVEMENT2"), and the French National Research Agency (ANR) Grant No. 09-BLANC-

0094 (project “SHREK”) and Grant No. 18-CE46-0013-03 (project “QUTE-HPC”).

### Appendix: Characterization of the grid flow

In the Appendix we shall use local velocity measurements performed by means of the wire heater in He I to compute the integral length scale $L_f$ and the turbulent intensity $I$ of the flow. There is a wealth of evidence that these large scale flow properties should remain largely unaffected by the transition from classical turbulence in He I to the He II quantum turbulent flow [18, 19]. With these primary quantities, we shall then estimate the Reynolds number and the so-called Kolmogorov dissipative length scale under the assumption of homogeneous and isotropic turbulence.

*a. Calibration of the wire heater* In He I the wire heater behaves as a conventional hot wire anemometer: As explained in Sec. VII B, the King's law is then very well suited to fit the electrical power dissipated in the wire heater as a function of the velocity. Here we use the raw King's law for calibration:

$$e^2 = C + Dv_\infty^{0.5}, \tag{A.1}$$

where the calibration constants $C$ and $D$ are determined using a polynomial fit of the mean voltage against the mean velocity in the tunnel.

*b. Turbulence intensity* Here we compute the turbulence intensity $I = v'/v_\infty$ where $v'$ is the standard deviation of the velocity.

The raw voltage records, and thus the velocity data, are affected by an uncorrelated base noise. Therefore, at low velocity, in which case the signal to noise ratio is small, the evaluation of the standard deviation of the velocity is not reliable. It is thus reasonable to use, for the turbulence intensity, the value found at the highest velocities:

$$I = v'/v_\infty \approx 2.6\%.$$

*c. Integral length scale* The longitudinal integral length scale is defined as follows:

$$L_f = \int_0^\infty \mathcal{R}_{xx} d\delta_x, \tag{A.2}$$

where $\mathcal{R}_{xx}$ is the autocorrelation coefficient of the longitudinal component of the fluctuating velocity $v'$ along the longitudinal axis $x$

$$\mathcal{R}_{xx}(\delta_x) = \langle v'(x)v'(x+\delta_x)\rangle / \langle v'^2\rangle. \tag{A.3}$$

Since we have access to the time series of the velocity, we use the Taylor hypothesis of frozen turbulence in order to transform temporal to spacial data through $x = \langle v\rangle t$.

The integral (A.2) converges to

$$L_f = 5.0 \pm 0.2\,\text{mm}$$

after a length scale $\delta_x$ that ranges between $2000L_f$ and $10000L_f$.

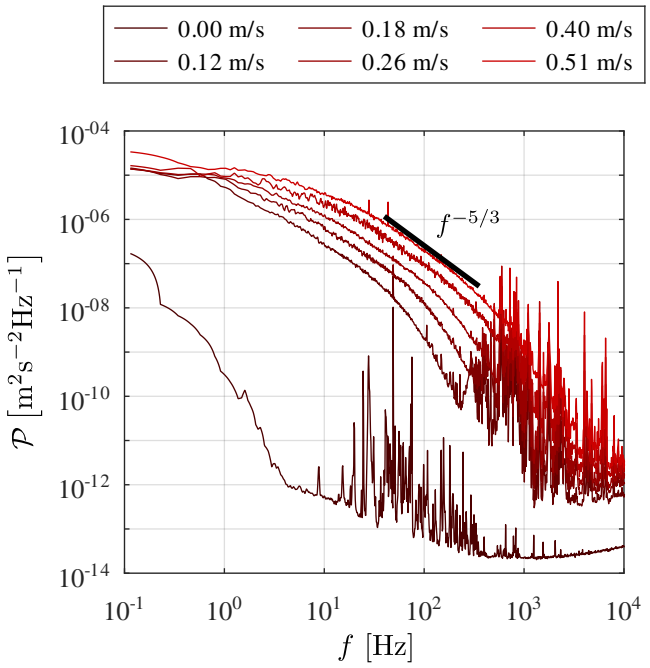


FIG. 16. Power spectral density of velocity time series as a function of the frequency at flow velocities $v_\infty$ ranging from $0\,\text{m}\,\text{s}^{-1}$ (dark red) to $0.51\,\text{m}\,\text{s}^{-1}$ (light red).

*d. Reynolds number and Kolmogorov dissipative length scale.* As the hot wire only gives access to one component of the velocity (streamwise), in order to compute the Reynolds number we first need to make an assumption on the isotropy and homogeneity of the flow. Then we can rely on the relation $R_\lambda = \sqrt{15\text{Re}_{Lf}}$ where $\text{Re}_{L_f} = I\langle v\rangle L_f/\nu$ (see e.g. Ref. [50]). For the largest velocities, this yields

$$R_\lambda \approx 230.$$

We can also evaluate the Kolmogorov dissipative length scale $l_\eta$ based on the definition $l_\eta/L_f = \text{Re}_{L_f}^{-3/4}$ which leads to

$$l_\eta \approx 10\,\mu\text{m}.$$

*e. General comments on spectral data in He I* In order to make general comments on the quality of the acquired fluctuating velocity time series, we can look at their power spectral density [PSD or $\mathcal{P}(f)$ hereafter] which has a very well known spectral signature in the considered grid flow.

As can be seen from Fig. 16, at all available velocities $v_\infty$ the PSD scales with the frequency reasonably well as $f^{-5/3}$. The extent of the inertial range in the frequency domain is about one decade, which is quite good considering that the length of the wire is only 10 times smaller than the large scale of the flow $L_f$. Finally we note that for nonzero velocities there appears a noise at frequencies above 200 Hz. We did not manage to determine the

source of this noise, but as it only introduces a small amount of energy at high frequency, we do not expect it to affect the conclusions of this paper.


[1] R. J. Donnelly, Phys. Today **62**, 34 (2009).
[2] C. F. Barenghi and N. G. Parker, *A primer on quantum fluids* (Springer, Cham, 2016).
[3] R. J. Donnelly, *Quantized Vortices in Helium-II*, Cambridge Studies in Low Temperature Physics (Cambridge University Press, Cambridge, 1991).
[4] S. Van Sciver, *Helium Cryogenics*, International Cryogenics Monograph Series (Springer, New York – Dordrecht – Heidelberg – London, 2012).
[5] I. M. Khalatnikov, *An Introduction to the Theory of Superfluidity* (Benjamin, New York – Amsterdam, 1965).
[6] D. Durì, C. Baudet, J.-P. Moro, P.-E. Roche, and P. Diribarne, Reviews of Scientific Instruments **86**, 025007 (2015).
[7] L. Saluto, D. Jou, and M. Mongiovi, Physica B: Condensed Matter **440**, 99 (2014).
[8] M. S. Mongiovì and D. Jou, Physical Review B **75**, 024507 (2007).
[9] E. Varga, Journal of Low Temperature Physics **196**, 28 (2019).
[10] S. Inui and M. Tsubota, Physical Review B **101**, 214511 (2020).
[11] E. Rickinson, C. F. Barenghi, Y. A. Sergeev, and A. W. Baggaley, Physical Review B **101**, 134519 (2020).
[12] Y. A. Sergeev and C. F. Barenghi, EPL (Europhysics Letters) **128**, 26001 (2019).
[13] W. Johnson and M. Jones, in *Advances in Cryogenic Engineering*, Advances in Cryogenic Engineering, Vol. 23, edited by K. D. Timmerhaus (Plenum Press, New York and London, 1978) pp. 363–370.
[14] B. Rousset, G. Claudet, A. Gauthier, P. Seyfert, P. Lebrun, M. Marquet, J.-L. Duchateau, *et al.*, Cryogenics **32**, 134 (1992).
[15] B. Rousset, G. Claudet, A. Gauthier, P. Seyfert, A. Martinez, P. Lebrun, M. Marquet, and R. Van Weelderen, Cryogenics **34**, 317 (1994).
[16] S. Fuzier, B. Baudouy, and S. W. Van Sciver, Cryogenics **41**, 453 (2001).
[17] S. Fuzier and S. W. Van Sciver, Cryogenics **48**, 130 (2008).
[18] J. Maurer and P. Tabeling, Europhysics Letters **43**, 29 (1998).
[19] J. Salort, C. Baudet, B. Castaing, B. Chabaud, F. Daviaud, T. Didelot, P. Diribarne, B. Dubrulle, Y. Gagne, F. Gauthier, A. Girard, B. Hébral, B. Rousset, P. Thibault, and P.-E. Roche, Physics of Fluids **22**, 125102 (2010).
[20] D. Duri, C. Baudet, P. Charvin, J. Virone, B. Rousset, J.-M. Poncet, and P. Diribarne, Review of Scientific Instruments **82**, 115109 (2011).
[21] G. Comte-Bellot and S. Corrsin, Journal of Fluid Mechanics **25**, 657 (1966).
[22] B. Rousset, P. Bonnay, P. Diribarne, A. Girard, J. M. Poncet, E. Herbert, J. Salort, C. Baudet, B. Castaing, L. Chevillard, F. Daviaud, B. Dubrulle, Y. Gagne, M. Gibert, B. Hébral, T. Lehner, P.-E. Roche, B. Saint-Michel, and M. Bon Mardion, Reviews of Scientific Instruments **85**, 103908 (2014).
[23] R. C. Kemp, Metrologia **28**, 327 (1991).
[24] Specification of bare chip Cernox thermometers (visited 12/2020): `https://www.lakeshore.com/products/categories/specification/temperature-products/cryogenic-temperature-sensors/cernox`.
[25] In principle, in the relation $T^n_{\rm chip} - T^n_\infty \propto \dot{Q}$ the temperature of helium at the chip interface, $T'_{\rm chip}$ should be used instead of $T_\infty$. However, such a correction would hardly alter the overlapping of the baselines since $T'_{\rm chip} - T_\infty < T_\lambda - T_\infty \ll T_{\rm chip}$ for (large) heat flux not exceeding $\dot{Q}_{\rm crit}$.
[26] M. J. Lighthill, Proceedings of the Royal Society (London) **A202**, 359 (1950).
[27] A. Acrivos, Physics of Fluids **3**, 657 (1960).
[28] D. C. Collis and M. J. Williams, Journal of Fluid Mechanics **6**, 357 (1959).
[29] G. B. Mardion, G. Claudet, and P. Seyfert, Cryogenics **19**, 45 (1979).
[30] C. E. Swanson and R. J. Donnelly, Journal of low temperature physics **61**, 363 (1985).
[31] A. Sato, M. Maeda, T. Dantsuka, M. Yuyama, and Y. Kamioka, AIP Conference Proceedings **823**, 387 (2006).
[32] G. K. Batchelor, *An Introduction to Fluid Dynamics* (Cambridge University Press, Cambridge, England, 2000).
[33] W. F. Vinen and J. J. Niemela, Journal of Low Temperature Physics **128**, 167 (2002).
[34] J. Salort, P.-E. Roche, and E. Lévêque, Europhysics Letters **94**, 24001 (2011).
[35] S. Babuin, E. Varga, L. Skrbek, E. Lévêque, and P.-E. Roche, Europhysics Letters **106**, 24006 (2014).
[36] P.-E. Roche, S. Babuin, E. Lévêque, and E. Varga, in *15th EuropeanTurbulence Conference proceedings*, 15th EuropeanTurbulence Conference 2015 (ETC15), edited by D. U. of Technology, Delft University of Technology (TU DELFT) (Delft University of Technology and European Mechanics Society (EUROMECH), Delft, Netherlands, 2015).
[37] J. J. Niemela, K. R. Sreenivasan, and R. J. Donnelly, Journal of Low Temperature Physics **138**, 537 (2005).
[38] R. J. Donnelly and C. F. Barenghi, Journal of Physical and Chemical Reference Data **27**, 1217 (1998).
[39] P.-E. Roche, C. F. Barenghi, and E. Leveque, Europhysics Letters **87**, 54006 (2009).
[40] J. T. Tough, Superfluid turbulence (North-Holland Publishing Company, Amsterdam, 1982) Chap. 3, pp. 133–219.
[41] H. Bénard, Comptes Rendus Academie des Sciences **147**, 839 (1908).
[42] V. Strouhal, Annalen der Physik und Chemie. Neue Folge, Band Bd. V, H. 10 , 216 (1878).
[43] R. Parker and M. C. Welsh, International Journal of Heat and Fluid Flow **4**, 113 (1983).
[44] T. D. Nguyen and E. Naudascher, Journal of Hydraulic Engineering **117**, 1056 (1991).
[45] T. von Kármán and H. Rubach, Physikalische Zeitschrift

**13**, 49 (1912).
[46] R. D. Blevins, Journal of Sound and Vibration **92**, 455 (1984).
[47] Empirically, the length scale $D = (L_s^{-1} + L_n^{-1})^{-1}$ or $\min(L_s, L_n)$ would fit better the observed $f_p(T)$ dependence.
[48] J. Salort, B. Chabaud, E. Lévêque, and P.-E. Roche, EPL (Europhysics Letters) **97**, 34006 (2012).
[49] V. S. L'vov, S. V. Nazarenko, and O. Rudenko, Phys. Rev. B **76**, 024520 (2007).
[50] G. K. Batchelor, *The theory of homogeneous turbulence* (Cambridge University Press, Cambridge, England, 1953).